International Journal of Plasticity 193 (2025) 104436



Contents lists available at ScienceDirect

International Journal of Plasticity

journal homepage: www.elsevier.com/locate/ijplas





Mechanistic origin of size effects in crystal plasticity: Strain gradients and other theories explained

Arya D. Nugraha, Gustavo M. Castelluccio *

Faculty of Engineering and Applied Sciences, Cranfield University, Cranfield, Bedfordshire MK43 0AL, United Kingdom

ARTICLE INFO

Keywords:
Crystal plasticity
Material independent parameters
Size effects
Dislocation structures

ABSTRACT

Mechanical properties–strength, fracture toughness, fatigue resistance–arise from the inherently multiscale nature of deformation and failure. Forces at the macroscopic level drive atomic-scale processes, which are regulated by mesoscale attributes such as grain size and dislocation structures. Thus, the engineering of novel materials requires a thorough understanding of complex interactions across multiple length scales. However, mechanistic explanations for size effects remain elusive in the literature. Instead, most modeling efforts have relied on phenomenological formulations, which offer limited predictive accuracy beyond their calibration domains.

This paper systematically explores mechanistic contributions to size effects to predict single- and poly-crystal mechanical responses. We identify three size-dependent mechanisms that can be incorporated into plastic deformation models to capture size effects in single- and poly-crystals for metals and alloys under tension, compression, and bending. The size-dependent algorithms do not introduce new phenomenological parameters but rely on material-invariant formulations that can be employed across single-phase FCC materials without recalibration. Notably, this understanding enables the tuning of microstructures for specific mechanical properties before manufacturing. The analysis further explains the relative contribution of size effects on isotropic and kinematic hardening as well as their significance for different crystallographic orientations. We further provide a physical interpretation for the origin of strain gradient theories and mechanistic size effects in the absence of geometry-induced strain gradients. We conclude by highlighting the coupling of mechanisms and their relative contributions at different strain levels.

1. Introduction

Microstructural refinement has a central role in engineering metallic materials given its capability to strengthen them without significantly degrading their fracture toughness. Microstructural hardening from mesoscales can be combined with atomic-scale solid solution strengthening and phase transformations to design novel, more resistant materials. However, the mechanisms by which microstructural attributes interact with plastic deformation are still not fully understood, and most modelling approaches rely on phenomenological rather than mechanistic formulations. Thus, the poor understanding of size effects hampers the integrated design of materials and hinders advances in failure prognosis.

The most common approach to predict grain size effects corresponds to the classical Hall-Petch relationship (HP) (Hall, 1951; Petch, 1953), which relates the stress (σ) with the grain diameter (D) through a power law, i.e.,

* Corresponding author.
E-mail address: castellg@cranfield.ac.uk (G.M. Castelluccio).

https://doi.org/10.1016/j.ijplas.2025.104436
Received 1 May 2025; Received in revised form 31 July 2025;
Available online 5 August 2025
0749-6419/© 2025 The Authors. Published by Elsevier Ltd. This is an open access article under the CC BY license (http://creativecommons.org/licenses/by/4.0/).

List of symbols

Greek symbols

α	Slip system
α_{LE}	Line tension coefficient
α_{Nye}	Nye tensor for gradient theory plasticity
β	El-Awady constant for initial wall spacing
$\Delta\tau$	Increase of shear stress compared to bulk material
∂S^{f}_{1212}	Partial derivative of finite Eshelby tensor
∂a	Partial derivative of a location in the Eshelby inclusion
$\partial \varepsilon^{pl}_{ik}$	Partial derivative of plastic strain
∂x_l	Partial derivative of a location in a material
ε^{*pl}_{12}	Plastic shear strain of Eshelby matrix
ε_p	Plastic strain
$\dot{\gamma}$	Shear rate
$\dot{\gamma}_w$	Shear rate of dislocation wall
$\dot{\gamma}_c$	Shear rate of dislocation inner core
γ^{eq}	Equivalent shear strain
γ_{max}	Shear strain in the most active slip system
$\gamma_{cottrell}$	Shear strain corresponds to Cottrell locks
γ_{hirth}	Shear strain corresponds to Hirth locks
γ^{cross}_{crit}	Critical cross-slip shear for stage III hardening
γ_p	Plastic shear strain
λ	Dislocation wall spacing/ cell diameter
λ_0	Initial dislocation wall spacing/ cell diameter
ΔG	Gibbs free activation energy
μ	Shear modulus at room temperature
μ_0	Shear modulus at 0 K
η	Aspect ratio of dislocation structures
η^{I}	Reference aspect ratio of Type I structure
η^{II}	Reference aspect ratio of Type II structure
η^{III}	Reference aspect ratio of Type III structure
ρ	Dislocation density
$\dot{\rho}$	Dislocation density rate of change
ρ_0	Initial dislocation density
ρ_{crit}	Critical dislocation density related to size effect dependency
ρ_{GND}	Geometry necessary dislocation density
σ	Normal Stress
$\boldsymbol{\sigma}$	Cauchy stress tensor
σ_0	Hall-Petch reference stress
$\boldsymbol{\sigma}^{PK2}$	Second Piola-Kirchoff stress
τ	Shear stress
τ_{eff}	Effective shear stress at atomic level
τ_{max}	Shear stress in the most active slip system
υ	Poisson's ratio
ω	Dislocation climb attempt frequency
ϕ_{CS}	Cross slip efficiency parameter
ψ	Maximum ratio of mean free path to effective size
ζ	Secondary slip system

Latin symbols

a	Distance of a point from the centre of Eshelby inclusion
A_{ii}	Dislocation self-interaction parameter
b	Burger's vector
B	Back stress
$\dot{B}$	Back stress rate of change
$\mathbb{C}$	Fourth rank elasticity tensor
C_{11}	Material elastic constant

C_{12}	Material elastic constant
C_{44}	Material elastic constant
C'	Gradient theory constant
d	Inclusion diameter in Eshelby inclusion problem
D	Effective material size (grain diameter, pillar diameter, beam half-thickness, etc.)
E	Elastic modulus
$\boldsymbol{E}^e$	Green strain tensor
$\boldsymbol{F}$	Deformation gradient
$\boldsymbol{F}^e$	Elastic deformation gradient
$\boldsymbol{F}^p$	Plastic deformation gradient
$\dot{\boldsymbol{F}}^p$	Plastic deformation gradient rate of change
F_0	Glide activation energy
f_w	Wall fraction of dislocation structures
f_w^I	Reference wall fraction of Type I structure
f_w^{II}	Reference wall fraction of Type II structure
f_w^{III}	Reference wall fraction of Type III structure
f_{Hill}^S	Hill factor
k	Hall-Petch constant
k_B	Boltzman constant
K_{struct}	Similitude constant
K_{multi}	Dislocation multiplication constant
l	Dislocation mean free path
$\boldsymbol{L}^p$	Isoclinic plastic velocity gradient
$\boldsymbol{m}$	Slip plane normal
n	Hall-Petch exponent
N_{sys}	Number of slip systems
p	Profile parameter for Gibbs free activation energy
q	Profile parameter for Gibbs free activation energy
R_0	Ratio of inclusion to matrix size in Eshelby inclusion problem
$\boldsymbol{s}$	Slip direction
S	Athermal stress
S_0	Peierls stress
S_{1212}	Eshelby tensor for shear
S_{1212}^f	Finite Eshelby tensor for shear
s_t^0	Thermal stress at 0K
t	Ratio of point of interest distance to matrix size in Eshelby inclusion problem
T	Temperature
v	Dislocation velocity
v_G	Cross slip characteristic frequency
V_{CS}	Cross slip activation volume
y_s^{edge}	Edge dislocation annihilation distance
y_s^{screw}	Screw dislocation annihilation distance

$$\sigma = \sigma_0 + kD^{-n}. \tag{1}$$

Li et al. (2016) used formal statistical testing to demonstrate that this equation offers no better predictive power over other formulations (e.g., logarithmic). Moreover, Dunstan and Bushby (2013) demonstrated that HP exponent carries large uncertainty and cannot be precisely determined through experimental fitting means. Indeed, several authors (Aghaie-Khafri et al., 2012; Bragg, 1942; Mathewson et al., 1916) have reported widely varying values for the parameter n, ranging from 0 to 1, with a few (Arzt, 1998; Hirth, 1972; Saada, 2005) agree with the traditional value of 0.5. The difficulties in agreeing on a single power coefficient result from shallow optimization functions prone to large errors from small fluctuations in the experimental data. Thus, the calibration of models without a mechanistic theory can be misleading and can conceal rather than reveal the underlying behavior (Dunstan and Bushby, 2013).

Other popular approaches correspond to gradient theories (Konstantinidis and Aifantis, 1998; Shu and Fleck, 1999; Smyshlyaev and Fleck, 1996), which have often been implemented in crystal plasticity finite element modelling (CPFEM) to predict size effects (Agius et al., 2022; Gu et al., 2021; Jiang et al., 2022). These approaches rely on phenomenological length scales, which are open for interpretation and inconsistent from model to model (Voyiadjis and Song, 2019). More practically, these length scales usually need recalibration and reinterpretation for each material (i.e., composition, microstructure), loading condition (i.e., monotonic, cyclic), or boundary condition (i.e., single crystal and polycrystal). The identification of the material length scale is controversial and cannot be done independently from the data it seeks to predict (i.e., stress-strain data with different grain size). These limitations suggest that the

material length scale conveys multiple mesoscale mechanisms that are coupled.

One mechanistic origin of grain size effect corresponds to pile-up theories, in which grain boundaries increase stress by forming pile-ups. Grain boundaries are normally strong obstacles to dislocations and in the majority of cases, they are impenetrable, the exception being low energy or low disorientation ($<10^{\circ}$), which is a minority of grain boundaries in random textures. Slip transmission may increase for small samples or grain sizes, for which the stress can be high enough, but is likely a second order effect (Imrich et al., 2014). Although the pile-up mechanism is plausible, it is not extensively found in experiments, especially in materials with medium to high stacking fault energy (SFE) such as Cu, Ni, and certainly Al; dislocations would preferably cross slip rather than pile up (Kuhlmann-Wilsdorf, 2002). Even if pile-ups are present, their extension tends to be much shorter in experiments than those required theoretically to justify the higher stresses observed. In reality, much of the modelling literature ignores these experimental arguments and overfit pile-ups models to match the experiments. As a result, current models have limited predictive power beyond the experimental set used for calibration and do not provide physical bases to distinguish size effects contributions, for example to isotropic or kinematic hardening.

Even if pile-ups are not present, grain boundaries or crystals free surfaces prevent dislocation free glide, reducing the average mean free path, and promoting further hardening from dislocation production. The reduction in mean free path has been proposed in Fourie (1968) as the dominant mechanism in crystals. This mechanism has been often cited in the literature (Dollar and Thompson, 1987; Rubio et al., 2019) by limiting the mean free path, but it is insufficient to predict size effects for the yield stress (Ashraf and Castelluccio, 2021).

Discrete dislocation dynamics (DDD) has provided physical insight into size effects through direct modelling of dislocations albeit at low strains and small specimens due to their high computational cost. For example El-Awady (2015), Jiang et al. (2019) and Zhang and Aifantis (2011) have utilized DDD understanding to predict size effects and demonstrated that the initial yield stress is affected by the grain size due to a change in the initial dislocation density. In particular, El-Awady (2015), performed a comprehensive analysis to understand and estimate grain and crystal size effects during monotonic loadings using 3D-DDD. They argue that a smaller grain size effectively increases the dislocation density while further work hardening increases the dislocation density from a minimum level controlled by the grain size. This argument is strikingly similar to that posed by Geometrically Necessary Dislocation theories, which argue that the reduction in grain size increases GND. Thus, it seems plausible that an inverse similitude relationship exists between the minimum attenable dislocation densities and grain size exists, either related total dislocation density or GNDs.

This paper proposes a mechanistic approach to rationalise the origin of size effect, explain prior theories, and distinguish isotropic and kinematic hardening contributions. We consider the substructure sensitive CPFEM model proposed for single phase FCC materials by Castelluccio and co-workers (Ashraf and Castelluccio, 2023; Castelluccio and McDowell, 2017; Dindarlou and Castelluccio, 2022). This approach is unique in mitigating parameter uncertainty by predicting the response of macroscopic single crystals and polycrystals of large grain size ($>100\mu m$) by means of material-invariant mesoscale parameters. Hence, we systematically review and reformulate the model hypotheses to predict the response of single- and poly-crystals up to 0.1 μm in size. Among three size-dominant mechanisms, one relates to the reduction in mean free path and another to the constraint of dislocation structures, which introduces strain gradients. A third mechanism relates to the initial dislocation density, which depends on the grain size through a material invariant similitude relationship. The results are validated for single crystals and polycrystal FCC metals and alloys, under tension and bending across different plastic strain levels. We further demonstrate that different mechanisms dominate at different plastic strain levels, which explains the partial success of prior models and enables independent parameterization of mechanisms. We conclude discussing the nature of the size effect, the role of non-equilibrum processes, and relating strain gradients to the constraint imposed by dislocation structures without phenomenological assumptions or additional parameterizations.

2. Substructure-sensitive crystal plasticity modelling

One major source of uncertainty in crystal plasticity corresponds to the identification of parameters, which has normally been addressed by simultaneous optimization of multiple coefficients. However, this approach results in large uncertainty due to the shallow objective functions, for which small changes in input data result in large changes in the optimum coefficients. Castelluccio and coworkers (Ashraf and Castelluccio, 2023; Castelluccio and McDowell, 2017; Dindarlou and Castelluccio, 2022) addressed this problem by proposing a substructure-sensitive CPFEM approach which relies on independent identification of parameters and unparallel validation at the meso- and macroscopic scales for single and poly-crystals. Their work has focused on identifying each parameter independently using various data sources ensuring physical meaning and avoiding overfitting. They have also demonstrated that models with parameters validated to single crystals can reproduce polycrystal response in the absence of grain size effects (typically grain size of hundreds of microns). Since these models do not consider size effects and they are only applicable for large crystals for which size effects are negligible, we seek to explore additional missing mechanisms that can capture size effects while maintaining the independent parameterization.

Hence, we proceed with a systematic review of the underlying hypotheses in CPFEM to identify their contribution to size effects. The crystal plasticity formulation considers a large deformation approach using the multiplicative decomposition of the deformation gradient, $\boldsymbol{F}$, into elastic and plastic components, $\boldsymbol{F}^e$ and $\boldsymbol{F}^p$, respectively,

$$\boldsymbol{F} = \boldsymbol{F}^e.\boldsymbol{F}^p. \tag{2}$$

The time derivative of $\boldsymbol{F}^p$, $\dot{\boldsymbol{F}}^p$, relates to the isoclinic intermediate configuration plastic velocity gradient ($\boldsymbol{L}^p$) and is computed as the sum of shear strain rate, $\dot{\gamma}^{\alpha}$, multiplied by the dyadic product of slip direction, $\boldsymbol{s}^{\alpha}$, and slip normal, $\boldsymbol{m}^{\alpha}$, of each slip system, α.

$$\dot{\boldsymbol{F}}^{p} = \boldsymbol{L}^{p}.\boldsymbol{F}^{p}, \tag{3}$$

with

$$\boldsymbol{L}^{p} = \sum_{\alpha=1}^{N_{sys}} \dot{\gamma}^{\alpha}(\boldsymbol{s}^{\alpha} \otimes \boldsymbol{m}^{\alpha}). \tag{4}$$

Green strain tensor, $\boldsymbol{E}^{e}$, could be expressed as a function of $\boldsymbol{F}^{e}$ as follows,

$$\boldsymbol{E}^{e} = \frac{1}{2}\left[(\boldsymbol{F}^{e})^{T}.\boldsymbol{F}^{e} - \boldsymbol{I}\right], \tag{5}$$

and the 2nd Piola Kirchoff stress then can be calculated by multiplying this tensor to a fourth rank elasticity tensor, $\mathbb{C}$:

$$\boldsymbol{\sigma}^{PK2} = \mathbb{C} : \boldsymbol{E}^{e}, \tag{6}$$

Finally, Cauchy stress is computed as,

$$\boldsymbol{\sigma} = \frac{1}{\det(\boldsymbol{F}^{e})}\left[\boldsymbol{F}^{e}.\boldsymbol{\sigma}^{PK2}.(\boldsymbol{F}^{e})^{T}\right]. \tag{7}$$

The plastic shear strain rate follows an Orowan relation and depends on the mobile dislocation density (ρ^{α}), Burgers vector (b), and average dislocation velocity (v) (Orowan, 1940), i.e.,

$$\dot{\gamma}^{\alpha} = \rho^{\alpha} b v, \tag{8}$$

in which

$$v = l\omega exp\left(\frac{-\Delta G}{k_B T}\right), \tag{9}$$

where l, ω, k_B, and T correspond to the mean free path, attempt frequency, Boltzmann constant, and temperature respectively. Gibbs free activation energy ΔG is estimated following the dislocation analysis from Kocks et al. (1975).

$$\Delta G = F_0\left(1 - \left[\frac{\tau}{S_t^0}\right]^{p}\right)^{q}, \tag{10}$$

in which τ is macroscopic shear stress informed from finite element solver, F_0 and s_t^0 being glide activation energy at 0 K and thermal stress while p and q being profile parameters. These parameters determine the thermal dependence of the yield stress, and they pertain to atomic unit processes that control energy barriers to dislocation. Since these processes are intrinsically atomic- rather than meso-scale, we assume that their parameterization does not depend on the grain size or the loading condition. This assumption ignores compositional or structural changes (e.g., vacancies, Cottrell clouds), induced by nearby free surfaces. We note that F_0 can be inferred from the stacking fault energy (SFE) (Ashraf and Castelluccio, 2021) while s_t^0 can be estimated from yield stress, indentation or atomistic simulations.

Combining Eqs. (8), (9), and (10), shear strain rate is expressed as:

$$\dot{\gamma}^{\alpha} = \rho^{\alpha} bl\omega\ exp\left(\frac{-F_0}{k_B T}\left\langle 1 - \left[\frac{\tau_{eff}^{\alpha}}{s_t^0 \frac{\mu}{\mu_0}}\right]^{p}\right\rangle^{q}\right) sgn(\tau^{\alpha} - B^{\alpha}), \tag{11}$$

$$\langle \Delta G \rangle = \begin{cases} 0, & \Delta G \leq 0 \\ G, & \Delta G > 0 \end{cases}, \tag{12}$$

where μ and μ_0 are the material shear modulus at temperature T and 0 K. While Eq. (11) describes an atomic level mechanistic, Eq. (13) bridges micro- to meso- level stresses with τ_{eff}^{α} and τ^{α} represents the local effective stress at atomic level and mesoscale stress calculated by finite element respectively while B^{α} and S^{α} represents back stress and athermal stress in each slip systems.

$$\tau_{eff}^{\alpha} = \langle |\tau^{\alpha} - B^{\alpha}| - S^{\alpha} \rangle \tag{13}$$

In polycrystalline materials, the back stress has intergranular and intragranular contributions, the former of which is captured by modelling grains explicitly. In single phase materials, the intragranular back stress arises from the localization of dislocations into sessile structures that behave as a composite material: high dislocation density immobile regions behave almost elastically and constrain the plasticity in the low dislocation density volume.

Castelluccio and McDowell (2017) developed a mechanistic formulation that quantifies back stress by explicitly accounting for the shape and size of dislocation structures. Hence, we defined back stress, B^{α}, as residual stress due to constraint of dislocation walls on an inner core (two-phase model, see Fig. 1). The rule of mixture relates the total plastic shear rate, $\dot{\gamma}$, as a function of wall fraction, f_w,

shear rate at wall, $\dot{\gamma}_w$, and at inner core, $\dot{\gamma}_c$:

$$\dot{\gamma}^{\alpha} = f_w \dot{\gamma}_w^{\alpha} + (1 - f_w)\dot{\gamma}_c^{\alpha}, \tag{14}$$

Since the wall dislocation density is much higher than at the core, plastic deformation is assumed negligible in the walls ($\dot{\gamma}^{w} \approx 0$). Annihilation mechanisms are still operative, and they affect the wall thickness by reducing its width as plastic deformation progresses. Hence, we assume that the wall only undergoes elastic deformation, and the back stress is calculated as the following,

$$\dot{B}^{\alpha} = \frac{f_w}{1 - f_w} \frac{2\mu(1 - 2S_{1212})}{1 + 4S_{1212} f_{Hill}^{S}} \dot{\gamma}^{\alpha} \tag{15}$$

in which S_{1212} is Eshelby tensor component for pure shear deformation and f_{Hill}^{S} is Hill factor following Berveiller and Zaoui (1978) (Eq. (16)). The Eshelby tensor maps the shear applied on an infinite domain to a spherical inclusion inside. However, as the grain or crystal sizes become comparable to that of dislocation structures, the approach breaks down. Hence, Eq. (15) lacks size effect contributions to the back stress from violating an infinite domain assumption.

$$f_{Hill}^{S} = \frac{3}{2}\frac{d\varepsilon_p}{d\sigma} = \frac{1}{2}\frac{d\gamma_p}{d\tau} \tag{16}$$

The athermal stress is defined as the total stress required to bow-out dislocations with respect to the dislocation-dislocation interaction strength expressed by dislocation line energy coefficient, α_{LE}, and colinear dislocation interaction parameter, A_{ii}:

$$S^{\alpha} = \alpha_{LE}\frac{\mu b}{2\lambda} + \mu b\sqrt{A_{ii}\rho^{\alpha}} + S_0^{\alpha} \tag{17}$$

With λ being the mean structure wall spacing and can be calculated through similitude with constant K_{struct} and shear stress in the most active slip system τ_{max},

$$\lambda = K_{struct}\frac{\mu b}{\tau_{max}}, \tag{18}$$

which does not depend on the crystal size and is temperature and material independent (Ashraf and Castelluccio, 2022; Lee and Nix, 2012; Sauzay and Kubin, 2011). We note that this formulation assumes that the intrinsic lattice Peierls stress in FCC materials is negligible and lacks a constant term ($S_0^{\alpha} \approx 0$).

The first term in Eq. (17) estimates the strength required to bow out dislocations from a dislocation wall while the second part describes the colinear dislocation interaction. Latent hardening interactions are captured by the formation of locks that refine the substructure, reduce the mean free path, and increase the back stress. Dislocation dynamics efforts (Gérard et al., 2013; Madec and Kubin, 2017) have shown that colinear dislocation interaction parameter (A_{ii}) are independent on the crystal size beyond a few microns in size. Hence, the hypotheses underpinning the athermal stress S^{α} formulation do not suggest that there is a missing size effect on the model form or parameters.

The calculation of the mobile dislocation density on each slip system, ρ^{α}, proceeds from estimating dislocation multiplication, annihilation and cross slip processes, i.e.,

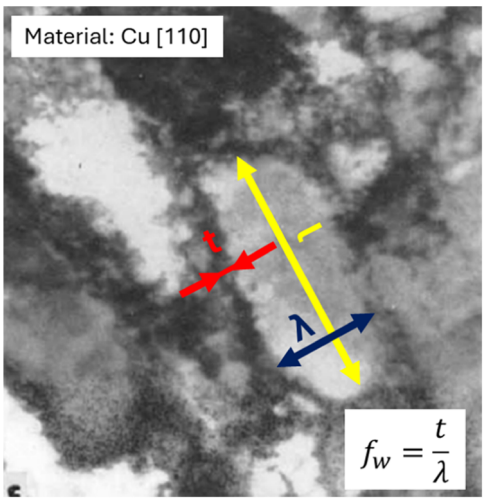


Fig. 1. TEM image of Copper [100] at 21 % tensile strain (Sard and Weil, 1970). Two different phases are present: wall (dark) and inner core (light). Wall fraction, f_w, is defined as the ratio between wall thickness, t, and cell size/ wall spacing, λ.

$$\dot{\rho}^{\alpha}=\frac{K_{multi}}{bl}|\dot{\gamma}^{\alpha}|-\frac{2y_s^{edge}}{b}\rho^{\alpha}|\dot{\gamma}^{\alpha}|-\frac{2\pi}{\mu b\lambda}\left|\dot{\tau}^{\alpha}_{eff}\right|_{Unload}+v_G\frac{\lambda}{\lambda_0}\left(\phi_{CS}\sum_{\zeta=1\ (\zeta\neq\alpha)}^{N}\rho^{\zeta}exp\left(-V^{\alpha}_{CS}\frac{\frac{\mu b}{4\pi y_s^{screw}}-|\tau^{\alpha}-B^{\alpha}|}{K_BT}\right)-(1-\phi_{CS})\sum_{\zeta=1\ (\zeta\neq\alpha)}^{N}\rho^{\alpha}exp\left(-V^{\zeta}_{CS}\frac{\frac{\mu b}{4\pi y_s^{screw}}-|\tau^{\zeta}-B^{\zeta}|}{K_BT}\right)\right) \tag{19}$$

in which K_{multi} is the dislocation multiplication constant, y_s^{edge} & y_s^{screw} are edge and screw dislocation annihilation distance, v_G, ϕ_{CS}, & V_{CS} are cross slip characteristic frequency, efficiency parameter, and activation volume, and α & ζ signifies the slip system. This approach relies on two dislocation substructure length scales: cell diameterwall spacing (λ) and mean free path (l). Eq. (19) relates the kinematic of glide with dislocation density on purely geometrical bases at the atomic unit process. Hence, we assume that the formulation and parameters are independent of the crystal size.

For monotonic loading, Dindarlou and Castelluccio (2022) identified three dislocation substructures— elongated cells (Type I and II) and equiaxed cell (Type III)— and defined the mean free path as the product of the structure wall spacing, λ, and the cell aspect ratio, η,

$$l=\eta\lambda. \tag{20}$$

This definition assumes that dislocation walls and grain boundaries are most likely impenetrable to mobile dislocations. Thus, this approach is strictly valid only for grains and crystals much larger than the structure wall spacing and needs to be revisited to incorporate size effects.

Following Estrin et al. (1998) and Müller et al. (1996), f_w and η are constants for Type III. For Type I & II, the saturated reference values (denoted by I, II, III in Eq. (22) & (23)) should be corrected with error function of the equivalent shear strain, γ^{eq}, divided by the typical equivalent shear strain of stage III hardening, γ_0^{eq} (Dindarlou and Castelluccio, 2022). Here, γ^{eq} is the weighed summation of shear strain accumulated on the most active slip system (γ_{max}), Cottrell lock ($\gamma_{cottrell}$), and Hirth lock (γ_{hirth}).

$$\gamma^{eq}=\gamma_{max}+\gamma_{cottrell}-\frac{1}{2}\gamma_{hirth} \tag{21}$$

$$\eta=\begin{cases}\eta^{I}\times[1+erfc(\gamma^{eq})],\ Type\ I\\ \eta^{II}\times[1+erfc(\gamma^{eq})],\ Type\ II\\ \eta^{III}=1,\ Type\ III\end{cases} \tag{22}$$

$$f_w=\begin{cases}f_w^{I}\times[1+erfc(\gamma^{eq})],\ Type\ I\\ f_w^{II}\times[1+erfc(\gamma^{eq})],\ Type\ II\\ f_w^{III},\ Type\ III\end{cases} \tag{23}$$

Dindarlou and Castelluccio (2022) also reported that- through systematic parameterization- these parameters are material invariant for FCC metals. We listed the relevant materials properties (pure metals and alloys) and meso-scale parameters in Table 1, Table 2, and Table 3 respectively, which were previously identified in the same paper.

2.1. Finite element modelling

The CP model was implemented to Abaqus/CAE standard through UMAT subroutine. The 3D model was based on a rectangular dog bone tensile specimen, containing 4000 linear brick elements with enhanced hourglass control (C3D8R) in the gage section. Each

Table 1
Material properties of pure FCC metals.

Parameter	Values		
	Cu	Ni	Al
Shear modulus at room temperature, μ (GPa)	45.0	80.0	28.0
Shear modulus at 0 K, μ_0 (GPa)	55.0	92.0	31.6
Screw dislocation annihilation distance, y^s_{screw} (nm)	40.0	40.0	80.0
Edge dislocation Annihilation distance, y^s_{edge} (nm)	2.0	2.0	4.0
Elastic constant, C_{11} (GPa)	161.0	249.0	115.0
Elastic constant, C_{12} (GPa)	119.0	155.0	62.0
Elastic constant, C_{44} (GPa)	75.0	114.6	31.0
Glide activation energy, F_0 (kJ/mole)	145	150	100
Thermal stress at 0 K, s_t^0 (MPa)	30	40	10

Table 2
Material properties of FCC alloys.

Parameter	Values		
	CrCoNi	SS316	AA5754
Shear modulus at room temperature, μ (GPa)	80.0	80.0	38.0
Shear modulus at 0 K, μ_0 (GPa)	92.0	92.0	41.6
Screw dislocation annihilation distance, y^s_{screw} (nm)	40.0	40.0	80.0
Edge dislocation Annihilation distance, y^s_{edge} (nm)	2.0	2.0	4.0
Elastic constant, C_{11} (GPa)	249.0	232.8	206.0
Elastic constant, C_{12} (GPa)	155.0	154.0	118.0
Elastic constant, C_{44} (GPa)	114.6	118.0	54.0
Glide activation energy, F_0 (kJ/mole)	170	180	125
Thermal stress at 0 K, s^0_t (MPa)	350	190	100

Table 3
Micro- and meso-scale material invariant parameters of FCC metals.

`Parameter	Values
Cross slip efficiency parameter, ϕ_{CS}	0.49
Reference type I wall fraction, fw_I	0.23
Reference type II wall fraction, fw_{II}	0.24
Reference type III wall fraction, fw_{III}	0.2
Reference type I aspect ratio, η_I	3.7
Reference type II aspect ratio, η_{II}	5.15
Reference type III aspect ratio, η_{III}	1.0
Critical cross slip strain, γ^{cross}_{crit}	0.003
Dislocation line energy coefficient, α_{LE}	1.0
Colinear dislocation interaction parameter, A_{ii}	0.1
Similitude constant, K_{struct}	9.0
Poisson's ratio, ν	0.3
Attempt frequency, ω	1.0E12

element represents a single grain with random grain orientations. Effective size, D, is assigned as a constant numerical value in each element, for instance, the size of an element does not determine the grain size in polycrystal.

We employed "Encastre" or fixed support boundary conditions on both end of the specimen, assuming a minimum gripper rotation and sliding. We replace axial support with displacement control at one end of the specimen as loading. Strain rate was kept in quasi-static region (0.01 to 0.1 s^{-1}). The geometry and boundary conditions are given in Fig. 2 and correspond to the mesoscale sample designed to test single crystal alloys (Lodh et al., 2023).

Unless otherwise stated, the engineering stress values reported in this paper refer to uniaxial normal stress in the x-direction, calculated by dividing the reaction force in the x-direction (at the fixed end) with the cross-section area of the gage section. Engineering strain is determined as the net displacement of the gauge section in the x-direction divided by its undeformed length. True stress and true strain are derived accordingly from these engineering values.

3. A mechanistic approach to size effects

Our approach aims to predict the behaviour of both single- and poly-crystals using the same model with the same set of parameters.

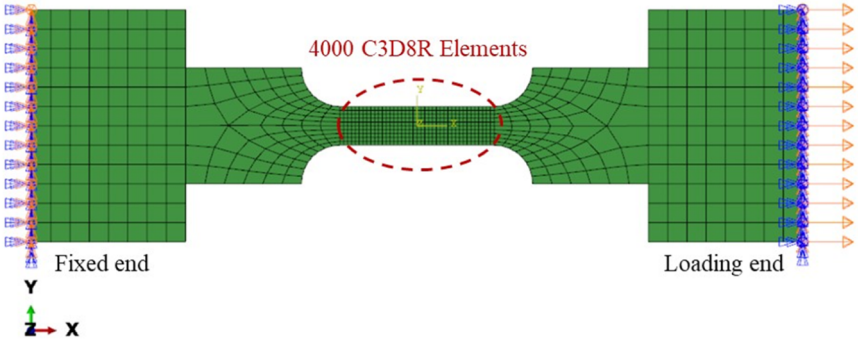


Fig. 2. Finite element model and boundary conditions used in this paper: C3D8R elements with fixed support and displacement loading.

Moreover, we seek to estimate each parameter independently using distinct experimental data, ensuring a one-to-one correlation between parameters and physical phenomena. Hence, the challenge is to identify mechanisms that inform parameters without relying on macroscopic tensile data (e.g., monotonic tests using different grain sizes). This approach differs from other theories since it prioritizes minimization of model input uncertainty through independent parameter identification. Next, we discuss different size-dependent mechanisms and their relation to substructure-sensitive CPFEM.

3.1. Changes in mean free path

Perhaps the simplest mechanistic size effect argument arises from the spacing of grain boundaries, which are mostly impenetrable obstacles to dislocations (except maybe for grain misorientation below 10° and small crystal size). Hence, a reduction of grain or crystal size reduces the distance that dislocations can travel freely, which results in a need to nucleate further dislocations. Therefore, ignoring the few cases of grain boundary dislocation transmission (which may be important for crack nucleation but less so for the bulk response), we can assume that the dislocation mean free path is a fraction of the crystal size, i.e.,

$$l < \psi D, \tag{24}$$

in which ψ estimates the fraction of a grain that a dislocation can travel before being arrested by a grain boundary in the absence of other obstacles. Hence, on average, dislocations would be able to travel at most half a grain diameter, which makes $\psi < 0.5$. In reality, core-mantle effects (Ghorbani Moghaddam et al., 2017) will likely make ψ slightly smaller than 0.5. Since the dislocation mean free path is also bounded by the dislocation structure spacing, we propose that the smaller of the two contributions governs the glide distance, i.e.,

$$l = \mathit{Min}(\psi D, \eta\lambda) \tag{25}$$

Since dislocation wall spacing evolves with strain, the limiting mean free path factor may change from the grain to the dislocation structure upon the refinement of the latter. Fig. 3 demonstrates that the mean free path controls size effects at intermediate strains for ψ ranging from 0.35 to 0.5. Since the stress difference is marginal with various ψ values, we assume that $\psi = 0.45$ to satisfy the $\psi < 0.5$ condition. The effects diminish as λ shrinks, activating the second part of Eq. (25), which recovers the mean free path definition in Castelluccio and McDowell (2017). The mean free path alone cannot explain certain experimental responses, particularly changes in yield stress. The same conclusion was reached by Ashraf and Castelluccio (2023), when comparing athermal and thermal contributions to hardening. In their case, single crystals show lower thermal stress than polycrystals because of grain size effects, even though they were considered with Eq. (25). Thus, this mechanism contributes by increasing isotropic hardening at intermediate strains due to size effects but causes minimal changes at yield or higher strains.

3.2. Back stress finite domain correction

Several researchers (Feaugas and Haddou, 2007; Gao et al., 2022; Haddou et al., 2001) have demonstrated that the back stress is also dependent on the grain or component size, which would limit the domain in which dislocation structures are embedded. Thus, the mechanistic model for back stress in Eq. (15) can be revisited assuming a finite domain. Following the elastic analysis from Li et al. (2007, 2005), we introduce the finite domain Eshelby tensor S^f_{1212} to replace S_{1212} in Eq. (15), which describes the strain distribution of an inclusion in a finite domain. Assuming a spherical domain, we introduced size related parameters *D, d,* and *a* which are, respectively, the domain diameter, inclusion diameter, and distance of the point of interest from the center of the inclusion illustrated by Fig. 4.

A finite domain affects the strain distribution inside the inclusion, which is no longer constant as in the classical Eshelby inclusion

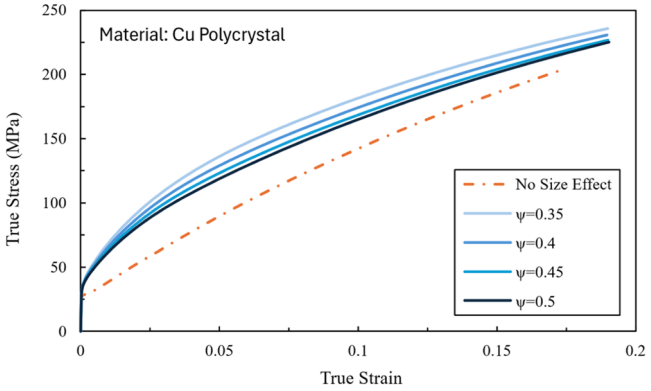


Fig. 3. CPFEM results exemplifying the influence of limiting ψ to 0.5, 0.45, 0.4, and 0.35 for Copper Polycrystal with average grain diameter of 5 μm. Parameters used for the simulation follows Tables 1 and 3 and has been validated in Dindarlou and Castelluccio (2022).

theorem, but results in strain gradients (Li et al., 2007). Thus, this mechanistic model effectively links size effects with strain gradients. Even in the absence of geometric-induced strain gradients, a reduction in the domain size increases the constraint to move dislocations within the substructure and simultaneously generates a strain gradient. Hence, the resulting Geometrically Necessary Dislocation (GND) densities and size effects are both a consequence of the additional constraint induced by dislocation walls compared to an infinite domain.

Assuming a finite elastic formulation, the Eshelby tensor as a function of the domain size ($R_0 = \frac{d}{D}$) and center position ($t = \frac{2a}{D}$) it follows (Li et al., 2007),

$$S^f_{1212}(R_0,t) = \frac{1}{1-\nu}\left\{\frac{4-5\nu}{15}\left(1-R_0^3\right) + \frac{7(5t^2-3)-20\nu t^2}{20(7-10\nu)}R_0^3\left(1-R_0^2\right) + \frac{3\nu t^2}{2(7-10\nu)}R_0^3\left(1-R_0^2\right)\left(\overline{x}_1\overline{x}_1+\overline{x}_2\overline{x}_2\right)\right\}. \tag{26}$$

Hence, a finite domain affects the Eshelby tensor and contributes to increasing the back stress in Eq. (15) while inducing strain gradients.

In the context of our model, we interpreted D as material effective size (grain size, pillar diameter, beam half-thickness, etc.) and d as dislocation mean free path (l). We then simplified this equation by taking the maximum value within the inclusion, which is in the center, $a = 0$, yielding:

$$S^f_{1212}(R_0,0) = \frac{1}{1-\nu}\left\{\frac{4-5\nu}{15}\left(1-R_0^3\right) - \frac{21R_0^3\left(1-R_0^2\right)}{20(7-10\nu)}\right\}. \tag{27}$$

The back stress correction considering the domain size heavily influences the stress-strain curve at medium to large strains as shown in Fig. 5 for Cu. The size effects reduces as loading progresses further for two main reasons: On the one hand, as dictated by the similitude (Eq. (18)), dislocation cell is inversely proportional to shear stress. Hence, as the stress increases, cells refine and progressively reducing ρ_0 (i.e., Eshelby tensor resembles more the infinite domain solution). On the other hand, dislocations tend to transition from elongated cell to equiaxed cell as loading progresses (Appendix A) further reducing the mean free path. We highlight that the proposed finite domain correction to the Eshelby tensor has no parameters that require calibration. Moreover, it is a size effect that contributes to the kinematic hardening.

3.3. Initial dislocation density

The HP model was initially introduced to relate the increase in yield stress with the reduction in grain diameter. However, the two mechanisms previously described do not increase yield stress: the mechanisms rely on profuse plasticity (a similar case occurs for strain gradient theories). On the contrary, the yield stress is associated with solid solution strengthening, which depends on the atomic unit process glide energy, and the initial dislocation density and structure, which tend to have large uncertainty in models. Hence, unless the initial dislocation density can be related to the crystal size (large model input obscures the understanding), we would conclude that the model form error dominates, and the formulation is incomplete as it is.

Notably, the pioneering gradient theories work (Fleck et al., 1994) proposed that the initial GND density increases as grain size decreases. More recently, El-Awady (2015) further showed that the minimum total dislocation density increases when the size is reduced. Fig. 6A, adapted from El-Awady's work, shows that initial cell size is dependent on the grain size and initial dislocation density until the critical point for a specific grain size (ρ_{crit}). Beyond this point, the cell size is no longer affected by the grain size and the relation between cell size and dislocation density is inversed (Eq. (28)). In other words, initial cell size will be the largest when $\rho_0 = \rho_{crit}$ is satisfied. We interpretate the macroscopic size effects as an effective increase in the initial dislocation density, part of which

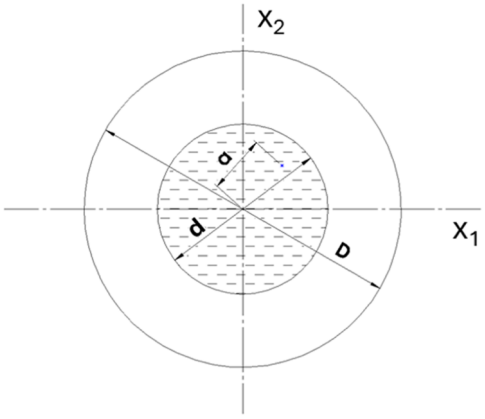


Fig. 4. Schematic of Eshelby finite formulation: an inclusion (hatched) inside a finite spherical domain.

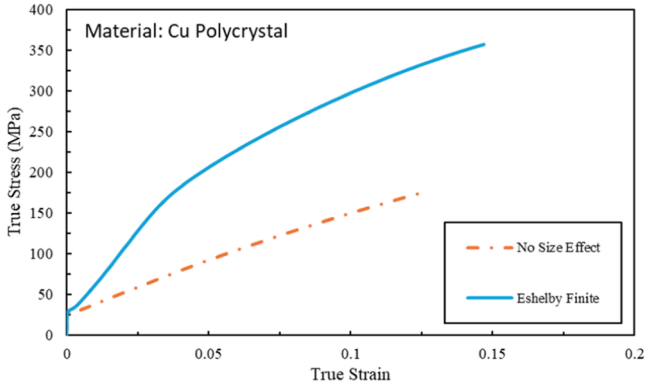


Fig. 5. CPFEM results exemplifying the stress increase with a finite domain Eshelby formulation on Cu Polycrystal with average grain diameter of 12 μm. Parameters used for the simulation follows Tables 1 and 3 and has been validated in Dindarlou and Castelluccio (2022).

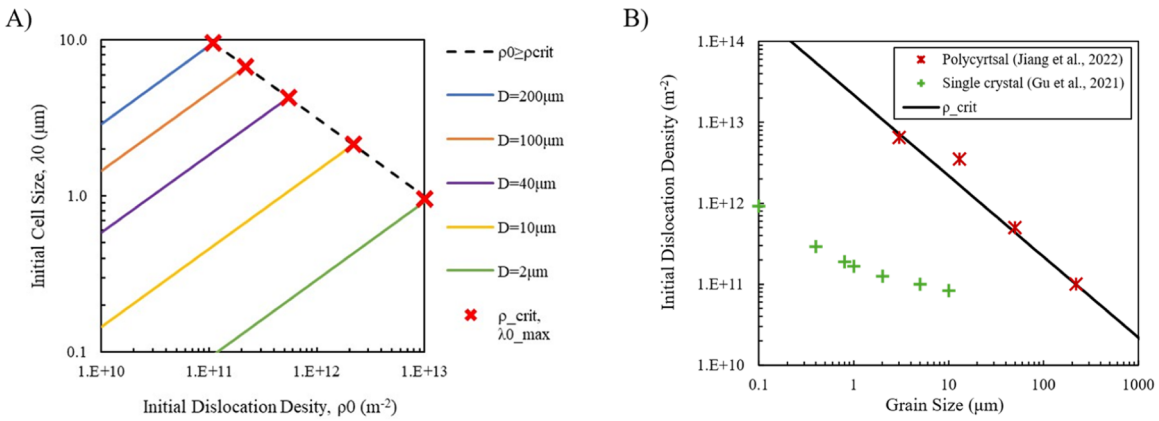


Fig. 6. DDD result on the correlation of size dependent initial dislocation density and initial dislocation length (El-Awady, 2015): A) Straight lines represent $\rho_0 < \rho_{crit}$ for various grain sizes, the black dotted line represents $\rho_0 \geq \rho_{crit}$ condition which is not size dependent. B) Initial dislocation density values used in Gu et al. (2021) and Jiang et al. (2022), plotted against ρ_{crit}.

corresponds to GNDS, which are only dominant at high strains. We note that assumptions still need to be made on the ρ_0 value, but under thermodynamic equilibrium, it should be higher for smaller samples/grains (El-Awady, 2015; Gu et al., 2021; Jiang et al., 2022). Additionally, if size effect is present, then the value should be less than ρ_{crit} as shown in Fig. 6B

Following Fig. 6A, the initial structure size can be described as,

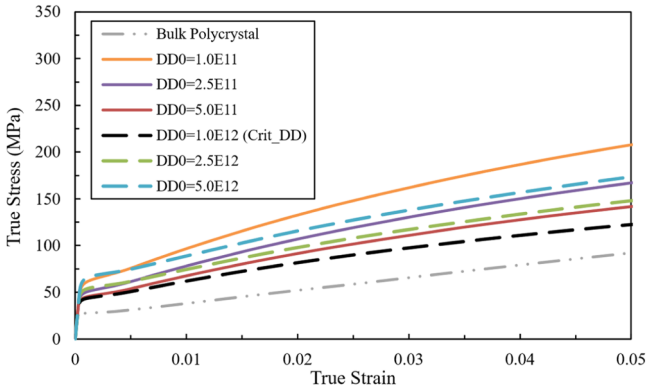


Fig. 7. Effect of varying initial dislocation density on Copper Polycrystal with average grain diameter of 12 μm. Straight lines represent $\rho_0 < \rho_{crit}$ while dotted lines represent $\rho_0 \geq \rho_{crit}$. $\rho_0 = \rho_{crit}$ produces the largest λ_0, thus the smallest yield stress increase.

$$\lambda_0 = \begin{cases} \dfrac{bD\sqrt{\rho_0}}{\beta}, & \rho_0 \leq \rho_{crit} \\ \dfrac{1}{\sqrt{A_{ii}\rho_0}}, & \rho_0 \geq \rho_{crit} \end{cases} \tag{28}$$

In which β is a constant with value of 1.76×10^{-3} (El-Awady, 2015). The initial dislocation cell size (λ_0) is then defined as the minimum value between Eq. (25) and (28):

$$\lambda_0 = \min\left(\frac{bD\sqrt{\rho_0}}{\beta}, \frac{1}{\sqrt{A_{ii}\rho_0}}, \psi D\right) \tag{29}$$

This contribution directly translates into isotropic, athermal hardening presented as bow-out stress in Eq. (17). Interestingly, Eq. (28) and (29) dictates that for any ρ_0 value below ρ_{crit}, stress is inversely proportional to square root of dislocation density. This means that Taylor hardening is violated as observed in various research looking at micron-scale specimens (Akarapu et al., 2010; El-Awady et al., 2009; Mayeur and McDowell, 2013; Zhuang et al., 2019). Furthermore, Taylor hardening is likely dominant in bulk engineering materials since Fig. 6 shows that the corresponding ρ_{crit} is significantly lower compared to nanocrystalline materials.

Fig. 7 presents the results from adding this size effect mechanism by varying the initial dislocation density for 12 μm copper polycrystal. Notably, $\rho_0=\rho_{crit}$ corresponds to the largest possible λ_0, which results in the lowest yield stress (black dotted line) due to the similitude (Eq. (17)). This condition, however, still gives a significant increase in yield stress compared to bulk polycrystal (grey line). Any initial dislocation density below or above ρ_{crit} would result in smaller initial cell size thus higher stress increase (colored lines).

3.4. Summary of size effect mechanisms

To summarize, we considered three contributions to size effect:

(1) Mean free path is limited to at least half of the effective material size. This reduces shear strain in Eq. (11), effectively increasing shear stress in intermediate strain level.
(2) When subjected to finite domain, an Eshelby inclusion will be additionally constraint and strain gradients, affecting the Eshelby tensor value. Back stress increases as a result through Eq. (15).
(3) Initial dislocation density affects the initial dislocation cell diameter/ wall spacing as a function of effective size. This contribution is a form of isotropic hardening and increases yield stress. The reduced initial cell diameter increases bow-out stress which contributes to the overall athermal stress (Eq. (17)).

These contributions are summarized in Table 4.

4. Comparison to experimental data

4.1. Application for single crystals

Among the three size effect contributions identified, the initial dislocation density has arguably the highest uncertainty and requires an input that depends on the material history. Even when multiple research (El-Awady, 2015; Gu et al., 2021; Jiang et al., 2022) agree that initial dislocation density increases at lower effective length, the parameterization still carries high uncertainty.

Pioneering efforts by Pippan's group (Kiener et al., 2006; Motz et al., 2005) reported an increase in yield stress but limited plastic hardening for copper [110] micro-bending tests with half-thickness from 0.5 μm to 3.75 μm (Fig. 8a). This response suggests that isotropic hardening (from initial dislocation density-cell size relation) is the dominant size effect. Mimicking these experiments, we implemented model for these specimens as shown in Fig. 8b considering the effective length scale (D) to be the beam half-thickness, $\psi = 0.45$, and calibrating the initial dislocation density to match the engineering stress. We follow the definition of engineering stress in Kiener et al. (2006) and Motz et al. (2005) specific for the bending case.

The optimal initial dislocation density to capture the experiment corresponds to,

Table 4
Driving mechanisms of size effect and their behaviors.

Contribution	Hardening	Effective Region	Stress Component
Mean free path limit	Kinematic	Intermediate strain	Shear stress
Eshelby finite domain	Kinematic	Intermediate - high strain	Back stress
Initial dislocation density	Isotropic	Yield	Athermal stress

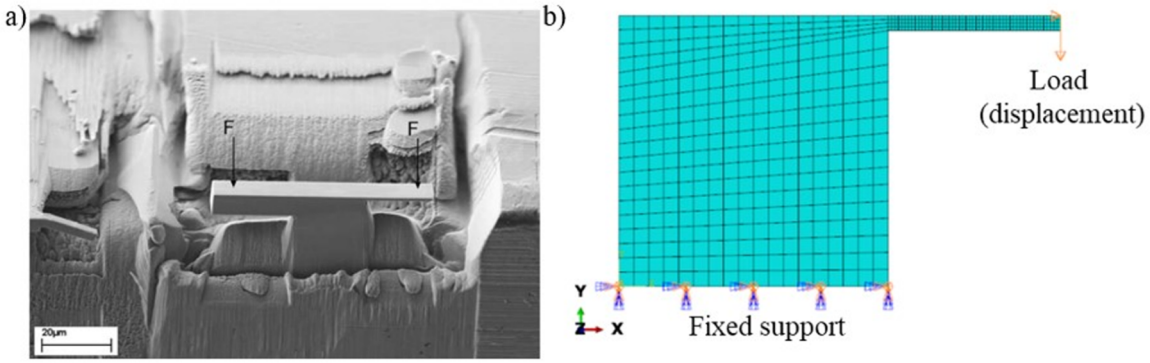


Fig. 8. Copper [110] micro-bending: a) experimental specimen (Motz et al., 2005) and b) finite element model.

$$\rho_{0,\,sx}(D) = \begin{cases} \dfrac{1e12}{D}, & D \geq 3.3\mu m \\ 3e11, & D \leq 3.3\mu m \end{cases} \tag{30}$$

The initial dislocation density increases with decreasing size up to around 3 μm in size, at which point we argue that the free surface moderates the dislocation density. Indeed, we hypothesize that this effect hinders dislocation increase as the free surface is acting as dislocation sink (Frank and Van der Merwe, 1949; Nabarro, 1947). Fig. 9 shows that using only the first part of Eq. (30) fails to capture the size effect of specimens with half-thickness smaller than 1.75 μm. On the other hand, moderating the dislocation density for sub-micron crystals results in additional isotropic strength through the bow-out stress (Eq. (17)). This also explains why gradient theory could not match the micro-bending size effect since it mostly induces kinematic hardening through back stress (Jiang et al., 2022).

Fig. 10 presents the force-displacement curve of the micro-bending specimen as well as comparison between micro-bending and micro pillar compression size effect. The copper micropillars are oriented along [111] direction, manufactured from the same bulk material as the micro-bending specimens (Kiener et al., 2006). We highlight we employ the same exact formulations and assumptions to predict both responses. Notably, we also use material invariant mesoscale parameters proposed by Castelluccio and coworkers (Dindarlou and Castelluccio, 2022).

Next, we compare the model predictions for CrCoNi and SS316 single crystal alloy experiments under compression. The model parameterization relies on mesoscale material invariant parameters proposed elsewhere (Dindarlou and Castelluccio, 2022) and the only calibration corresponds to the composition-dependent thermal stress (s_t^0), which was estimated to be 350 MPa for CrCoNi to match the experimental yield stress in macroscopic polycrystal. The initial dislocation density also follows that in Eq. (30). Fig. 11 presents the comparison of models and experiments for bulk sample with assumed average grain/ specimen size of 1 mm and single crystal micropillars with diameters of 2 μm to 0.5 μm oriented along [100] and [102] for CrCoNi and 3 μm to 6.5 μm for the [111] oriented SS316. The model predicts both single- and poly-crystals in small and large samples without requiring any recalibration. We highlight that the experimental difficulties in running small scale tests results in large experimental uncertainty, so a closer matching to

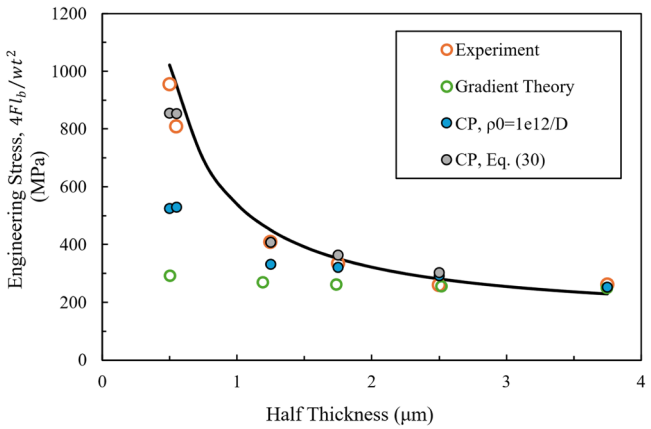


Fig. 9. Cu [110] micro-bending stress comparison between experiment (Motz et al., 2005), gradient theory, and crystal plasticity model: initial dislocation density plateaus near sub-micron region, inducing more isotropic hardening through bow-out stress. Bending engineering stress was calculated as a function of reaction force in vertical direction (F), bending length (l_b), beam width (w), and thickness (t).

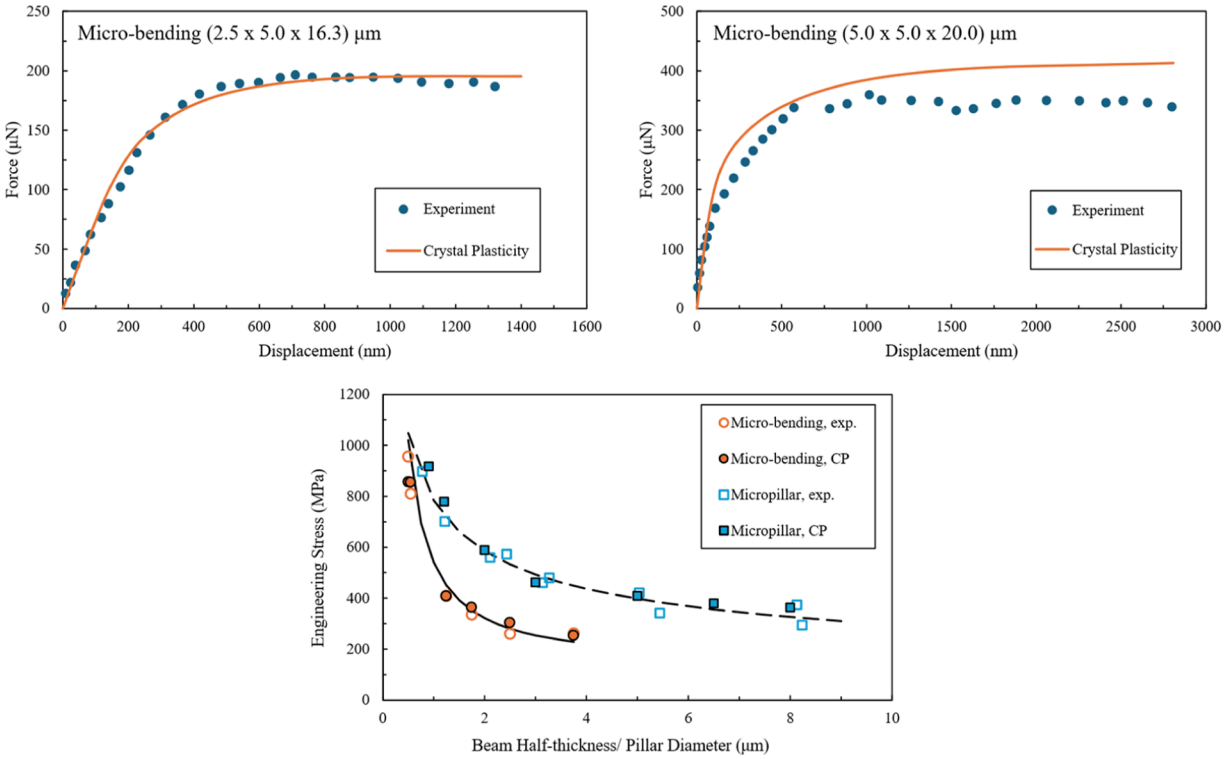


Fig. 10. CP model and experiment (Kiener et al., 2006; Motz et al., 2005) comparison: (Top) force-displacement curve of copper [110] micro-bending. (Bottom) size effect comparison to Cu [111] micropillar compression.

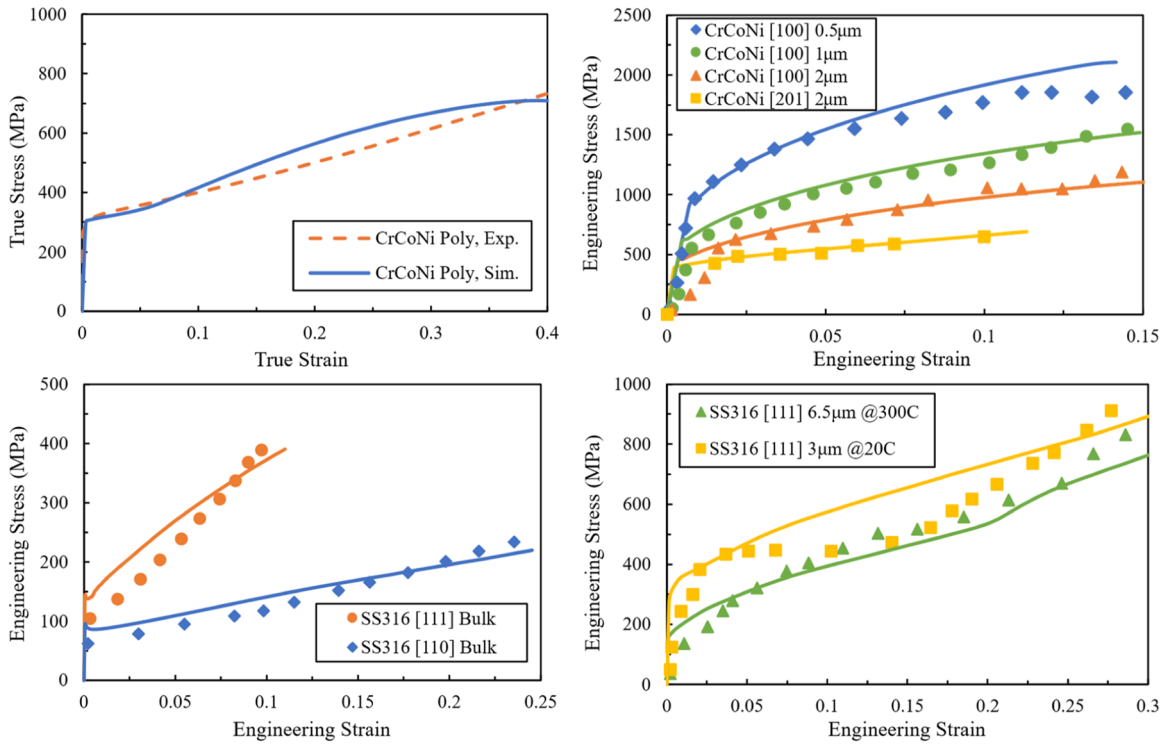


Fig. 11. CP prediction (lines) compared to experiments (dots) for CrCoNi and SS316 (Scherer et al., 2024; Xiao et al., 2020; Yan et al., 2023). s_t^0 was calibrated with polycrystal and bulk single crystals data respectively. Macroscopic grain sizes are assumed to be 1 mm in diameter.

experiments would probably be the result of overfitting. Furthermore, the model manages to reproduce the stress-strain behavior even when the SS316 micropillars were tested in different temperatures. These results support that size effects have a dominant athermal component, at least for crystals around and above 1 μm.

Next, Fig. 12 compares the model prediction to single crystal experimental results from various authors and different materials. Notably, normalized stresses for different single crystals fall in a single trend for both models and experiments for specimen sizes ranging from 40 μm to 0.2 μm. We note that experimental data points do not fall in a single trend because stresses were measured at different strain levels. Nevertheless, the modeling approach predicts the experimental trends robustly at each strain level. The blue vertical line represents the transition into high "surface effect" regime in which Eq. (30) describes ρ_0 as size independent (constant). These results for metals and alloys with different orientation demonstrate that the same size effect mechanisms operate among FCC materials with similar dislocation structures.

4.2. Back stress contribution to gradient based size effect

A decrease in grain or specimen size imposes a constraints on dislocation cells, such that the strain inside these cells is no longer constant, contrary to the result of the original Eshelby theory. Consequently, smaller sizes result in strain gradients within the dislocation cell, which can be estimated by taking the derivative of the Eshelby tensor component S^f_{1212}, i.e.,

$$\frac{\partial S^f_{1212}(R_0, D, a)}{\partial a} = \frac{2aR_0^3(R_0+1)(R_0-1)(7+2\nu)}{D^2(1-\nu)(10\nu-7)} \tag{31}$$

So that,

$$\frac{\partial \varepsilon^{pl}_{ik}}{\partial x_l} = \varepsilon^{*pl}_{12}\frac{\partial S^f_{1212}(R_0, D, a)}{\partial a} \tag{32}$$

In which ε^*_{12} is the applied strain on the effective medium. The strain gradient can then be related to the GND density (Voyiadjis and Song, 2019),

$$\rho_{GND} \approx \frac{1}{b}\left|\frac{\partial \varepsilon^{pl}_{ik}}{\partial x_l}\right| \tag{33}$$

In which the term inside the bracket is strain gradient or Nye tensor, α_{Nye} (Nye, 1953).

Fig. 13 presents the strain gradient and back stress inside an inclusion computed from Eq. (32) and (15) respectively. Large crystals or grains result in no strain gradients, recovering the classical Eshelby inclusion theorem and a constant back stress value. But for smaller crystals a strain gradient is induced with a consequent increase in back stress at the center of the inclusion.

Since the proposed size effect arises from the dependence of the Eshelby tensor on the domain dimensions, we argue that strain gradients and GNDs result from this additional constraint and correlate with the strengthening effect. Furthermore, gradient theory approaches (Ashby, 1970; Jiang et al., 2022) have directly correlated GND to back stress, consistent with our Eshelby finite domain

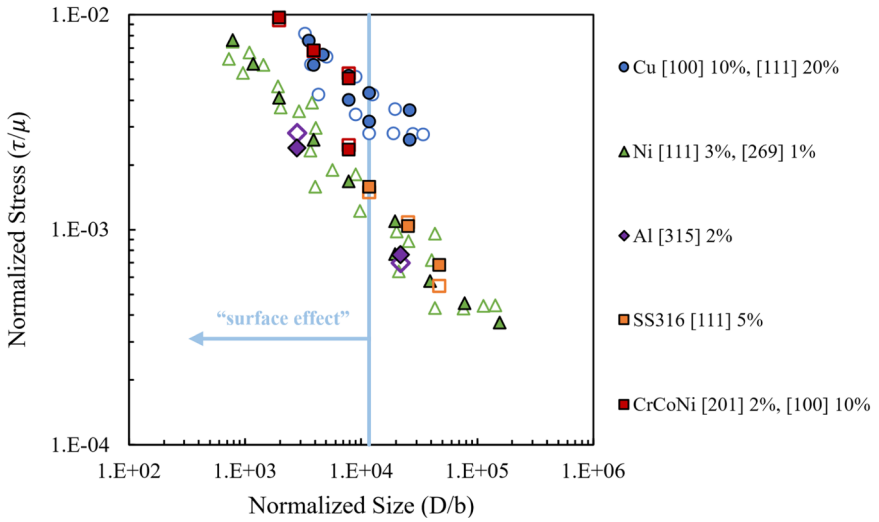


Fig. 12. Shear stress normalized with shear modulus for various single crystals. Strain levels are annotated next to the corresponding crystal orientation. Full dots represent CP results while hollow dots are experimental values reported in Dou and Derby (2009), Frick et al. (2008), Kiener et al. (2008,2006), Ng and Ngan (2008), Scherer et al. (2024), Uchic et al. (2009), Xiao et al. (2020) and Yan et al. (2023). Blue vertical line signifies the transition of Eq. (30). (For interpretation of the references to color in this figure legend, the reader is referred to the web version of this article.).

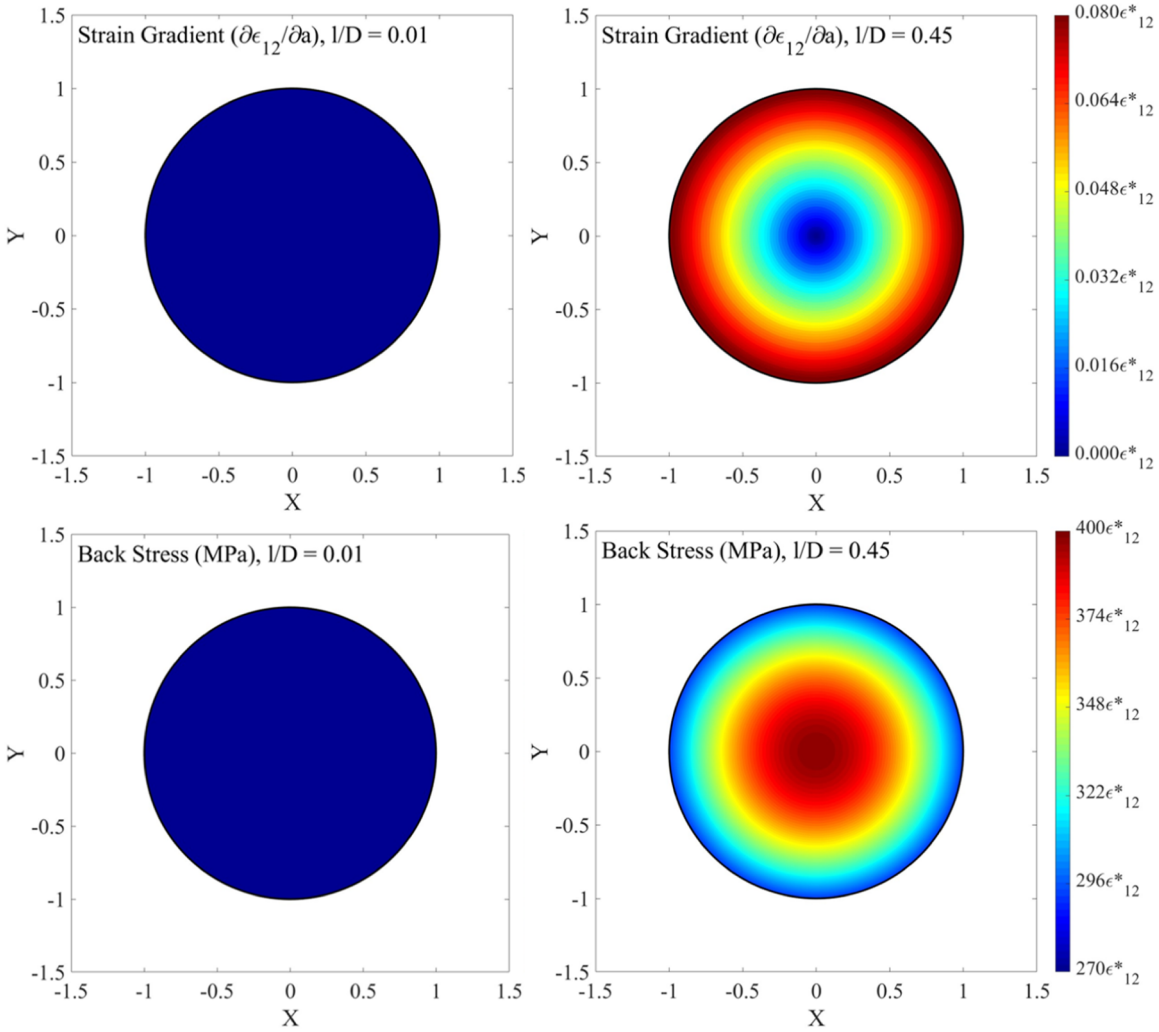


Fig. 13. Strain gradient inside an inclusion explained by Eshelby inclusion theorem: inclusion strain should be constant inside an infinite domain. As the domain shrinks, it restrains the inclusion, inducing strain gradient thus increasing back stress. The back stress is calculated for Cu with dislocation wall fraction of 0.2 and hill factor of 0.001.

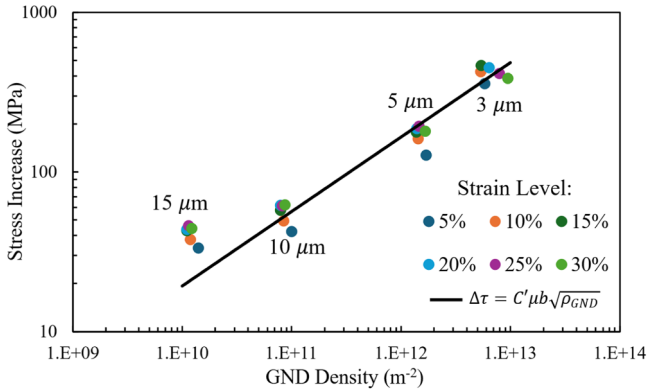


Fig. 14. Stress increase as a function of GND density: hardening due to Eshelby finite domain (dots) recovers classical gradient theory size effect (straight line) with C' value of 3.3. Data points with the same sizes form clusters along the theoretical line.

contribution. To assess the relationship between GNDs and size effects, we simulated a SS316 single crystal oriented along the [111] direction. The specimen sizes ranged from 300 μm (reference) down to 3 μm, including 15 μm, 10 μm, and 5 μm. Note that this analysis considers only the size effect contribution from the Eshelby finite domain. The results in Fig. 14 demonstrate that the stress increase due to size effect is proportional to the square root of GND density (Fleck et al., 1994), such that,

$$\Delta\tau = \tau_D - \tau_{ref} \approx C'\mu b\sqrt{\rho_{GND}} \tag{34}$$

With C' corresponds to a dimensionless constant in unity order (Fleck et al., 1994).

We recovered a C' value of 3.3 without explicitly embedding a gradient theory formulation into the model, consistent with classical literature (Fleck et al., 1994). Notably, this Taylor-type of relation, in which the stress increase is proportional to the square root of GND density has been extensively used in the literature. Hence, we provide a mechanistic explanation for the origin of this relation rather than prescribing it. Moreover, this approach allows independent parameterization of the gradient theory constant, since it depends on the additional constraint imposed by the size-dependent Eshelby tensor.

Similarly, we can explore the relationship predicted by the model between the structure length scale and the dislocation density. Some authors (Oudriss and Feaugas, 2016) reported that the dislocation structure dimension follows a similitude relation with the square root of dislocation density for equiaxed cell structure, which is compared in Fig. 15. Notably, the model predicts the same relation as in experiments, even when it has not been explicitly informed. Hence, Figs. 14 and 15 demonstrate that the model captures multiple mesoscale responses found in experiments.

4.3. Assessment of polycrystals

Fig. 16 compares models and experiments for multiple pure metals and alloys at room temperature (Cu, Ni, Al, SS316, AA5754) using the exact same model and material-invariant mesoscale parameterization. The grain size effect is mostly pronounced at intermediate strain levels (~5–10 % strain) mainly from the dislocation back stress constraint and reduction in dislocation mean free path.

The initial dislocation densities required to match the experiments are proportional to those proposed in Eq. (30) but are higher than those of the single crystals. Since engineering materials have complex thermomechanical processes, it is unlikely that single- and poly-crystals would have the same initial dislocations densities significantly (Koizumi et al., 2022; Wang et al., 2020). However, these uncertainties are also present in single crystals as experimental data shown in Fig. 12 since Eq. (30) captures the average experimental value. We quantify initial dislocation density uncertainty by taking experimental data at <5 % strain since ρ_0 is the dominant size effect contributor in this regime. Next, a 95 % confidence interval can then be established, and we use the CP model to capture the upper and lower bound as shown in Fig. 17.

Results shows that the 95 % confidence interval and polycrystals follow the same trend as shown in Fig. 18 and fall below the ρ_{crit} line. We also found that initial dislocation densities used in gradient theory plasticity for polycrystals (Jiang et al., 2022) and DDD for single crystals (El-Awady, 2015; Gu et al., 2021) follow similar trends. Thus, these results suggest that scaling Eq. (30) can describe the initial condition of thermomechanical processing.

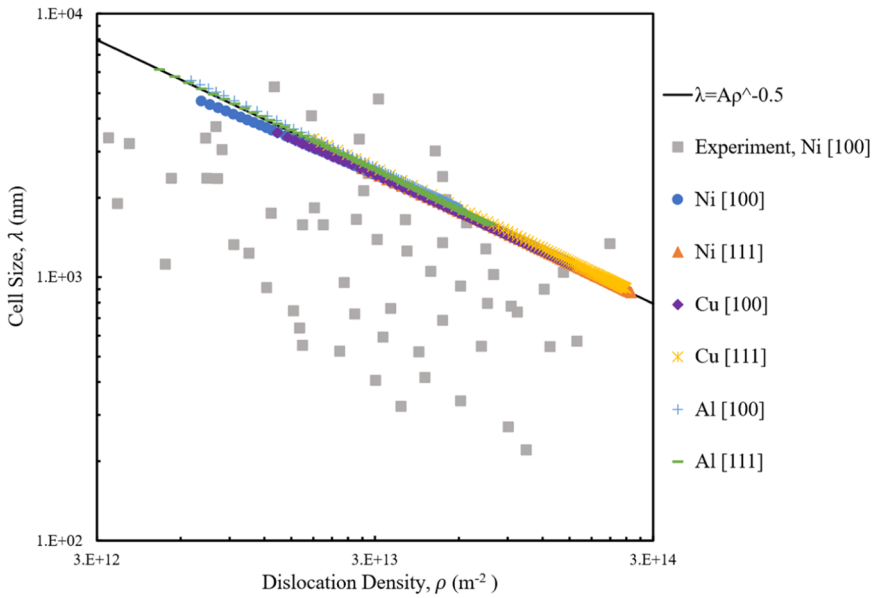


Fig. 15. Cell size evolution as a function of dislocation density: CP results are within range and recover correlation proposed in Oudriss and Feaugas (2016).

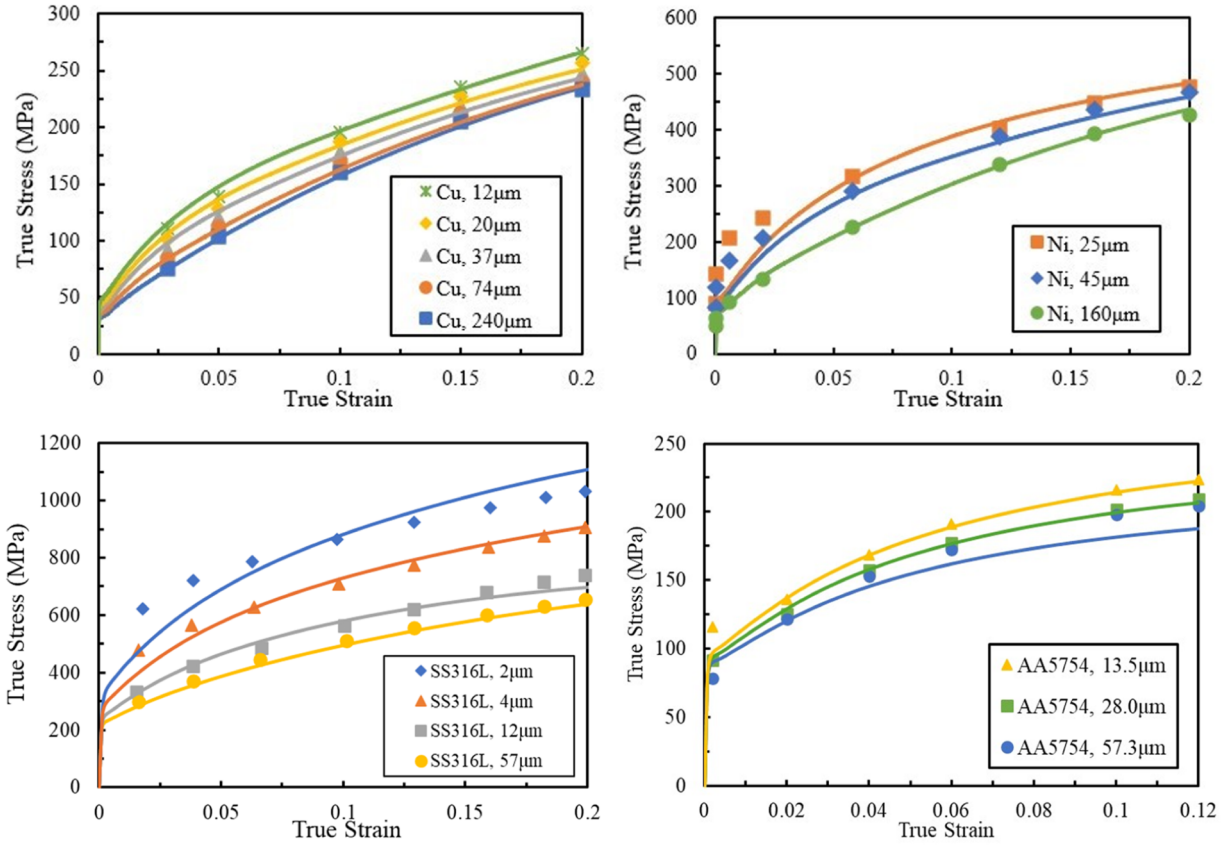


Fig. 16. CP model prediction for various polycrystals: the proposed framework is predictive for both single and poly crystals (Feaugas and Haddou, 2003; Hansen and Ralph, 1982; Lloyd and Court, 2003; Qin et al., 2019).

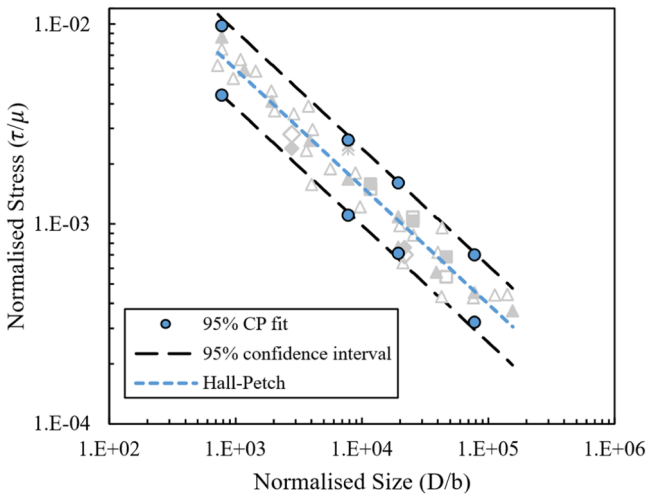


Fig. 17. 95 % confidence interval of experimental data assessed below 5 % strain. CP with modified ρ_0 was used to capture the lower and upper bound of the distribution.

5. Discussion

This paper explores mechanistic strategies from micro- and meso-scale levels to predict the response of single- and poly-crystals with robust parameterizations. The starting point is the substructure-sensitive crystal plasticity model, validated for large crystals

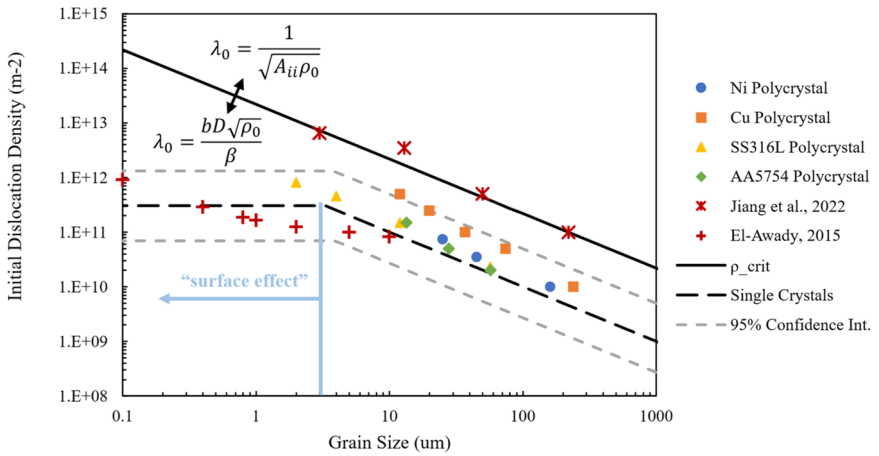


Fig. 18. Initial dislocation density values used in this research and (El-Awady, 2015; Jiang et al., 2022): polycrystals have higher dislocation density compared to Eq. (30) as an artefact of manufacturing processes. All the values fall below the critical dislocation density line, signifying that the strength of these specimens should be size dependent. Uncertainties regarding initial dislocation density value were quantified as the 95 % confidence interval bounds.

or grains without size effects, and independently parameterized using mesoscale, material invariant parameters. Next, we systematically revised the underlying assumptions to incorporate mechanisms that can explain the responses of metals and alloys across different sizes. We identified three mechanisms contributing to size effects related to model form and model input uncertainty: limiting the dislocation mean free path to about half the crystal or grain size; incorporating an Eshelby tensor for a finite domain; and considering an initial dislocation density that depends on the crystal size.

Most modelling efforts lack a robust strategy to parameterize the initial conditions (e.g., no systematic comparison with experiments prior to testing), especially for engineering materials that have undergone complex thermomechanical work hardening. Thus, the lack of systematic understanding of the initial conditions results in model overfitting. For example, (Rubio et al., 2019) assumed a simple model that reduces the mean free path, forcing higher dislocation production to match the kinematic condition imposed by crystal plasticity. As a result, the authors reproduce some hardening effects due to the grain size at the expense of changing the similitude constant. However, similitude has been argued to be material independent within the experimental uncertainty (Sauzay and Kubin, 2011). Thus, the approach by (Rubio et al., 2019) is incomplete, as it does not predict the increase in yield stress as expected from our analysis in Fig. 3. Similarly, their validation covers a relatively narrow range of grain sizes— with no single crystals— and lacks a strengthening effect on yield stress as well as the additional constraint from dislocation cells, which diminishes with increasing stress; this results in differing slopes between models and experiments (Rubio et al., 2019). This exemplifies how uncertainties from multiple mechanisms become dominant in different conditions, and that model validation requires a plethora of data to compare, which are often unavailable. Therefore, identifying trends common to families of materials is a useful strategy to enrich datasets and mitigate uncertainty when such data are lacking.

CPFEM and DDD results in Fig. 18 demonstrate agreement in scaling the initial dislocation density with crystal size for sizes above a few microns. Perhaps the most striking aspect is that the inverse relationship between dislocation density and square root of the grain size observed in single crystals can be scaled to predict the response of metallic materials with thermomechanical histories. This suggests that the inverse relationship between dislocation density and crystal size corresponds to an intrinsic similitude relationship resulting from thermodynamic equilibrium. Indeed, the refinement of the microstructure requires an increase in dislocation density to account for the changes in configurational entropy and achieve thermodynamic equilibrium (McDowell, 2024a; McDowell and Liu, 2025). Thus, for materials at or near equilibrium during manufacturing routes (slow casting, thermomechanical recrystallization, annealing, etc.), we can infer their initial dislocation density from simple grain size estimation as a means to reduce model input uncertainty. Processes far from equilibrium require understanding of the degree of correlation (McDowell, 2024b, 2024c) to estimate the configuration entropic contributions affecting the dislocation similitude relationship with crystal size. For example, microstructures produced through highly non-equilibrium processes (electrodeposition, equal channel angular extrusion, etc.) can result in very high dislocations densities above the single crystal line in Fig. 18. However, any subsequent thermal process introduced to enlarge grains will likely be close to equilibrium, so the changes in grain size and dislocation density will follow a square root relation (for grain size above a few microns). Thus, manufacturing processes that are close to equilibrium will satisfy the square root similitude relation in Fig. 18 while processes far from equilibrium can results in dislocation densities much higher and uncorrelated to the grain size. In theory, dislocation densities can be predicted if the entire thermomechanical history, both in equilibrium or not, is modeled starting from the solidification process. However, this is normally impractical, inaccessible and a grand challenge in most cases.

In the context of continuum finite element implementation, plasticity formulations assume dislocation glide is bound within each element. With enough mesh refinement, this assumption can be inaccurate, especially at the early stages of deformation, in which dislocation structures are more widely open and dislocation can glide long distances. If the dislocation mean free path is larger than the elements but not significantly different than that on the contiguous elements, we can assume that element state variables are repre-

sentative of the conditions outside the element. However, if the state variable differs significantly among contiguous elements (e.g., under large geometry-induce strain gradients), this assumption breaks down and we can expect ψ vary within the grain. This contribution can be avoided by considering elements that are larger than the structure or making ψ a function of the mean free path gradient. These effects correspond to another mechanistic contribution associated with geometry-induce gradient properties that need to be accounted for when considering elements sizes much smaller that the dislocation mean free path. In reality, some of the mesh dependences associated with size effect in geometries with grain are related to the locality of models and the lack of convective terms in dislocation glide beyond its neighbors. These effects die out with increased strain as dislocation mean free paths get shortened and more likely to stay within the element. Hence, in many cases the uncertainty associated with the lack of dislocation convection across elements is not dominant.

The interpretation of sessile dislocation structures constraint on dislocation glide using a finite-domain Eshelby theorem has resulted in a mechanistic understanding of strain gradients not induced by sample geometry. The Taylor-type relationship for gradient theories results from the increase in stress induced by higher cell constraint (change in Eshelby tensor) and the intrinsic similitude relationship between stress and dislocation densities. This suggest that self-hardening coefficients, A_{ii}, in Eq. (17) and Taylor factor in gradient theories (Eq. (34)) are not independent parameters.

With the model being predictive for both single and polycrystals, we can also clarify the relative contribution of size effect to isotropic or kinematic hardening for different crystal orientations. We chose [123] and [110] represent single slip and [100] and [111] for multiple slip. Fig. 19 presents notable differences among crystals beyond 10 % strain for the larger size (30 μm) in which [111] and [100] experience less hardening compared to the others.

Fig. 20 presents the back stress and athermal stress comparison of the 30 μm single crystals and the bulk (millimeter size). Here, it is evident that multiple slips crystals undergo back stress cross-over. This behavior corresponds to the delay in transitioning to equiaxed cell structure for single slip. These crystals have a longer mean free path, thus higher back stress increase through Eq. (15) and (27). Athermal stress increase also decays as the loading progresses for [111] and [100] samples due to higher slip activity compared to [123] and [110]. Through similitude (Eq. (18)), the shrinking rate of λ becomes higher in these orientations, causing the bow-out effect to be converged with the bulk eventually. We interpret these as a possible explanation to the variations of size effect in polycrystals: a moderately {111} textured SS316L reported in Feaugas and Haddou (2003) showed closer resemblance with multiple-slip single crystals in contrast with its untextured counterpart (Li et al., 2022).

The reduction of hardening, however, is not observable in the 5 μm and 1 μm specimens. Fig. 21 shows that the back stress increase for smaller materials, e.g. micropillars presented in Fig. 12, is enough to compensate for any stress cross-over. The decay of bow-out stress is also not present: Fig. 22 shows the initial cell size is small enough for $D = 5$ μm that the shrinkage is negligible for either single- or multiple-slips. We argue that these factors cause materials in these length scales to have relatively constant size effect with respect to strain.

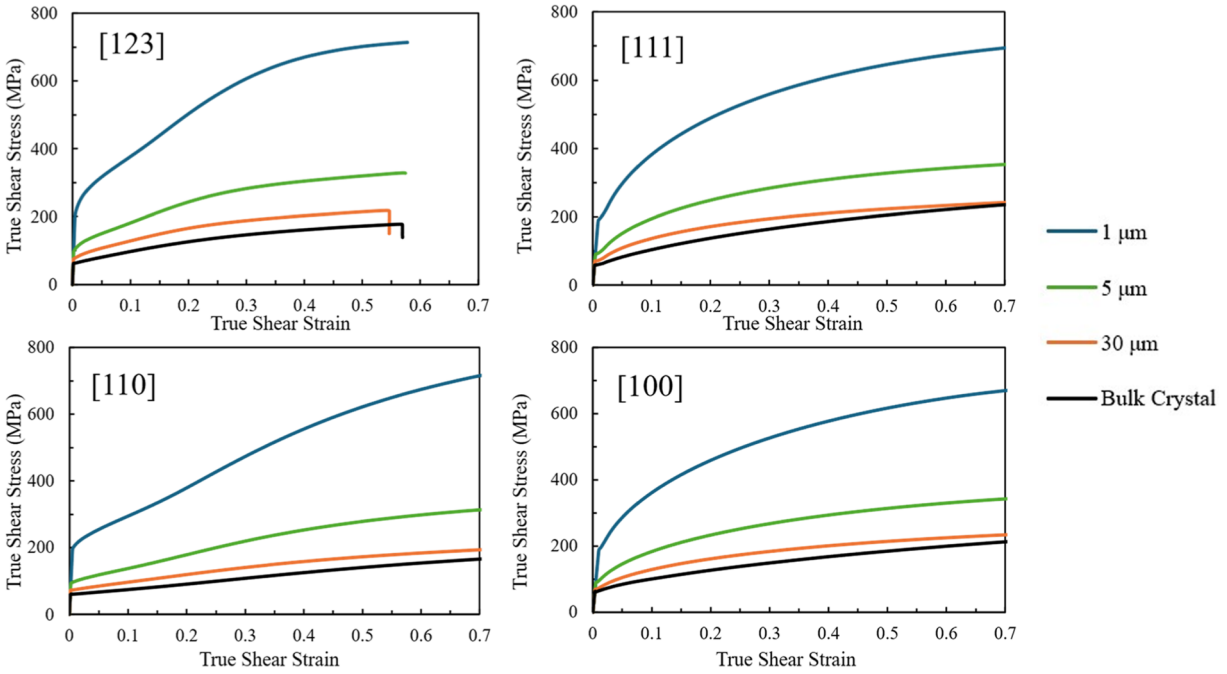


Fig. 19. Shear stress-shear strain curve of SS316 single crystals aligned for single (left) and multiple slip(s) (right) with various sizes: crystals oriented for single slip are more sensitive to size effect in $D \geq 30$ μm region.

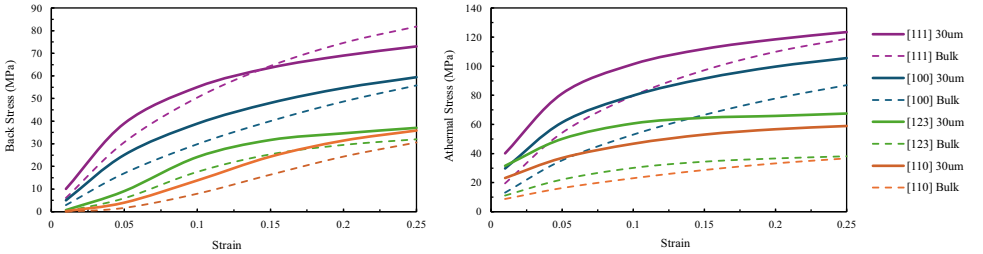


Fig. 20. Back stress and athermal stress contributions to size effect: back stress cross-over is not present in single slip crystals due to the delayed transformation to equiaxed cell dislocation sub-structure.

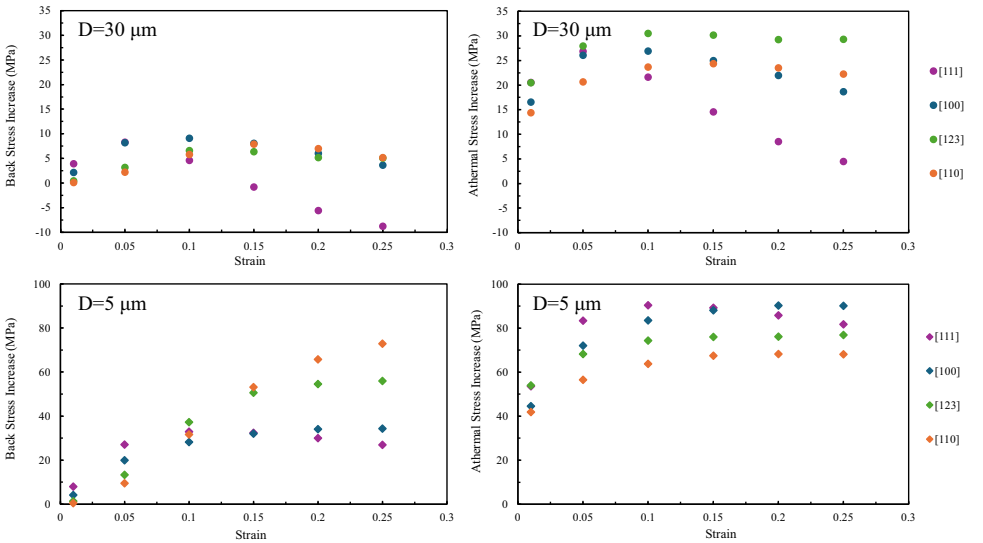


Fig. 21. Back stress and athermal stress increase (from bulk) of 30 μm and 5 μm samples. The size effect does not decay at smaller length scale.

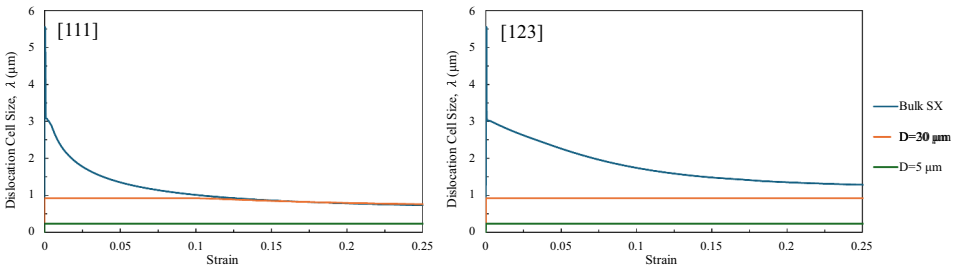


Fig. 22. Higher slip activity in materials oriented for multiple slips, in this case [111], causes dislocation cell to shrink at a higher rate: athermal bow-out stress of 30 μm sample converges with the bulk.

6. Conclusion

This paper presents a review of size effects theories for mechanical properties and proposes a mechanistic approach capable of explaining previous theories. Notably, we demonstrate that strain gradient theories arise from the increased constraint of glide within dislocation structures, and the resulting stress follows a Taylor-type relation. We further propose that an inverse similitude relation exists between the square root of the dislocation density and grain/crystal size up to about 1 μm. This relation is an intrinsic property from thermodynamic equilibrium, and thermomechanical history can be scaled to represent this up to a critical value (ρ_{crit}), beyond which dislocation density becomes independent of the grain size. We further argue that at or below approximately 1 μm, dislocation density is moderated by free surfaces or grain boundaries, and experiments can be captured by assuming constant initial dislocation densities.

In addition to advancing the mechanistic understanding of size effects, this paper presents a fully validated crystal plasticity model

capable of predicting the mechanical response of single- and poly-crystals of varying sizes. This model does not introduce any new parameters but instead leverages material invariant parameterizations. Hence, the approach only requires scaling the initial dislocation density and calibrating F_0 and s_t^0 (the former via the stacking fault energy, and the latter through experiments or atomistic simulations). Thus, parameterization is greatly simplified, and the model can be employed to design microstructures or predict the response of materials with minimum or potentially no experimental data.

CRediT authorship contribution statement

Arya D. Nugraha: Writing – review & editing, Writing – original draft, Methodology, Data curation. **Gustavo M. Castelluccio:** Writing – review & editing, Supervision, Project administration, Methodology, Funding acquisition, Formal analysis.

Declaration of competing interest

The authors declare that they have no known competing financial interests or personal relationships that could have appeared to influence the work reported in this paper.

Acknowledgement

The authors greatly appreciate the support from the US Naval Nuclear Laboratory.

Appendix

We characterized monotonic dislocation sub-structure into Type I, Type II, and Type III with the latter being equiaxed cell (Dindarlou and Castelluccio, 2022). For the structure to transform into Type III, the cross-slip strain should surpass a critical value which is more likely to be found in crystals oriented for multiple slips. Type I and Type II is defined by the amount of Cortell and Hirth locks. The flowchart for substructure determination is shown in Fig. 23.

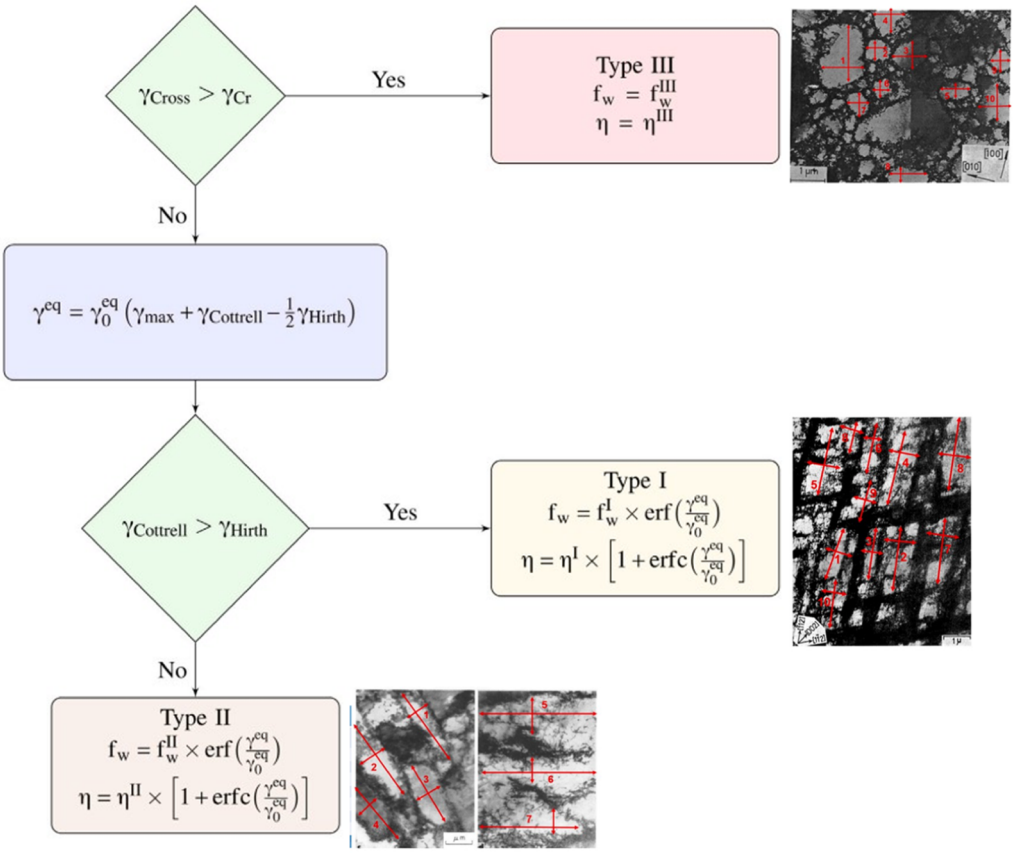


Fig. 23. Flow chart for identifying dislocation sub-structure in monotonic loading (Dindarlou and Castelluccio, 2022) with the corresponding structure TEM images (Kawasaki, 1974; Mughrabi et al., 1986; Sard and Weil, 1970).

In (Dindarlou and Castelluccio, 2024), the Authors simplified the determination process by assuming Type I and Type II structures

to be the same. However, we found that both approaches yield comparable results as shown in Fig. 24, thus we kept the old approach as the latest approach has only been published by the time we finalized this paper. A note should also be added regarding K_{struct} reported in (Dindarlou and Castelluccio, 2024), which has approximately half the value reported in this paper and (Dindarlou and Castelluccio, 2022). This is due to the different τ_{max} definition in that specific paper ($\tau_{max,24} = \tau_{max}/2$). Shall the same definition was used; the K_{struct} values will be in the same order of magnitude (8.1 and 9.0).

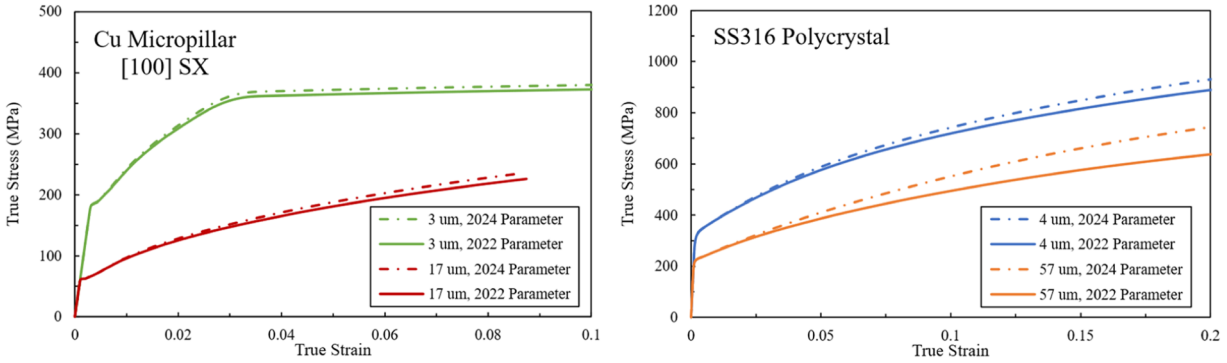


Fig. 24. Stress-strain response comparison of the old (Type I $\neq$ Type II) and latest (Type I = Type II) approaches.

The polycrystal finite element model has several assumptions:

1. Each element is treated as a single grain with distinct crystallographic orientations.
2. A single set of synthetic crystallographic orientations with no distinct texture generated from MTEX (Hielscher and Schaeben, 2008) is used for all material.
3. Grain size is a numerical constant, average value is assigned to all elements.

While assumption #1 reduces computational cost, the others follow the lack of details in the experimental literature. Indeed all of them could affect the macroscopic response of the polycrystal (although moderately) and the CP model could capture these effects given availability of the data. We note that Assumption #1 has been discussed previously (Dindarlou and Castelluccio, 2022).

Assumption #2 determines the about 10 % of stress-strain response of a material. We give an example of silver experimental data taken from (Carreker, 1957). The CP model was unable to capture the exact behavior of the material with the generic crystallographic orientations. However, as shown in Fig. 25, as we imbue synthetic [111] texture we get a closer match to the experiment. We stress that this data was not included in the main article due to the absence of the real EBSD data.

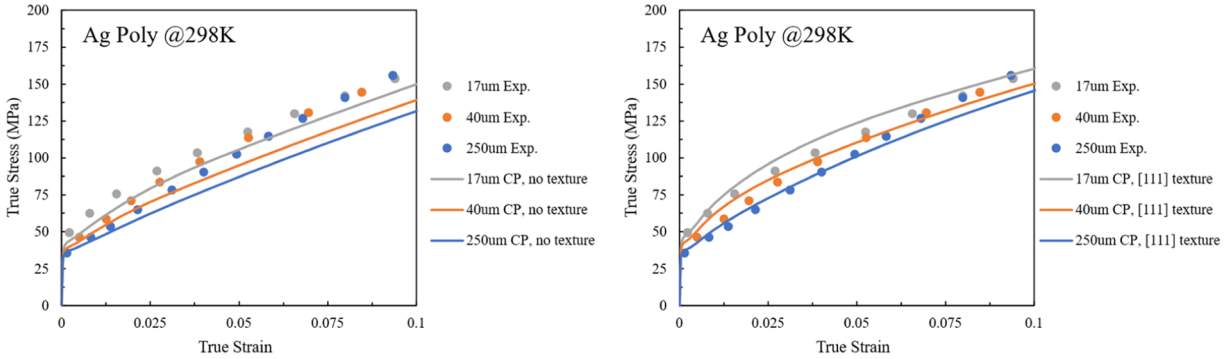


Fig. 25. The CP model with synthetic [111] dominated texture (right) captures experimental data from (Carreker, 1957) better compared to generic orientations we used for every other material (left). However, EBSD data are mostly absent from experimental literatures.

Assumption #3 has a negligible effect to the bulk stress-strain response. Below we compare the use of the average grain size value and a realistic grain size distribution. However, we hypothesized that grain size distribution could have a bigger impact on localization of plastic deformation and damage.

Fig. 26

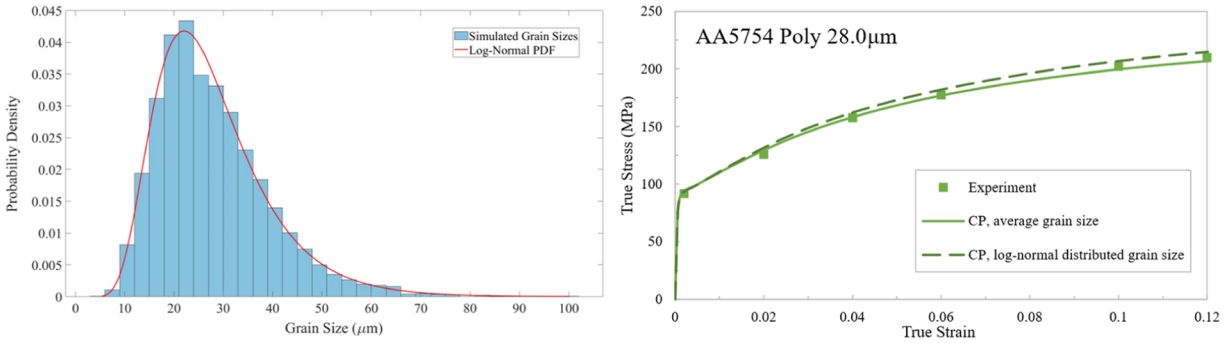


Fig. 26. Comparison of using average grain size value and realistic grain size distribution as CP input: the change in stress-strain curve is negligible for monotonic loading. Experimental data taken from (Lloyd and Court, 2003).

Data availability

Data will be made available on request.

References

Aghaie-Khafri, M., Honarvar, F., Zanganeh, S., 2012. Characterization of grain size and yield strength in AISI 301 stainless steel using ultrasonic attenuation measurements. J. Nondestr. Eval. 31, 191–196. https://doi.org/10.1007/s10921-012-0134-z.

Agius, D., Kareer, A., Mamun, A.Al, Truman, C., Collins, D.M., Mostafavi, M., Knowles, D., 2022. A crystal plasticity model that accounts for grain size effects and slip system interactions on the deformation of austenitic stainless steels. Int. J. Plast. 152, 103249. https://doi.org/10.1016/j.ijplas.2022.103249.

Akarapu, S., Zbib, H.M., Bahr, D.F., 2010. Analysis of heterogeneous deformation and dislocation dynamics in single crystal micropillars under compression. Int. J. Plast. 26, 239–257. https://doi.org/10.1016/j.ijplas.2009.06.005.

Arzt, E., 1998. Size effects in materials due to microstructural and dimensional constraints: a comparative review. Acta Mater. 46, 5611–5626. https://doi.org/10.1016/S1359-6454(98)00231-6.

Ashby, M.F., 1970. The deformation of plastically non-homogeneous materials. Philos. Mag. 21, 399–424. https://doi.org/10.1080/14786437008238426.

Ashraf, F., Castelluccio, G.M., 2023. History and temperature dependent cyclic crystal plasticity model with material-invariant parameters. Int. J. Plast. 161, 103494. https://doi.org/10.1016/j.ijplas.2022.103494.

Ashraf, F., Castelluccio, G.M., 2022. On the similitude relation for dislocation wall thickness under cyclic deformation. Mater. Sci. Eng. A 840, 142972. https://doi.org/10.1016/j.msea.2022.142972.

Ashraf, F., Castelluccio, G.M., 2021. A robust approach to parameterize dislocation glide energy barriers in FCC metals and alloys. J. Mater. Sci. 56, 16491–16509. https://doi.org/10.1007/s10853-021-06376-1.

Berveiller, M., Zaoui, A., 1978. An extension of the self-consistent scheme to plastically-flowing polycrystals. J. Mech. Phys. Solids. 26, 325–344. https://doi.org/10.1016/0022-5096(78)90003-0.

Bragg, L., 1942. A theory of the strength of metals. Nature 149, 511–513. https://doi.org/10.1038/149511a0.

Carreker, R.P., 1957. Tensile deformation of silver as a function of temperature, strain rate, and grain size. JOM 9, 112–115. https://doi.org/10.1007/BF03398466.

Castelluccio, G.M., McDowell, D.L., 2017. Mesoscale cyclic crystal plasticity with dislocation substructures. Int. J. Plast. 98, 1–26. https://doi.org/10.1016/j.ijplas.2017.06.002.

Dindarlou, S., Castelluccio, G.M., 2024. Optimization of crystal plasticity parameters with proxy materials data for alloy single crystals. Int. J. Plast. 174, 103894. https://doi.org/10.1016/j.ijplas.2024.103894.

Dindarlou, S., Castelluccio, G.M., 2022. Substructure-sensitive crystal plasticity with material-invariant parameters. Int. J. Plast. 155, 103306. https://doi.org/10.1016/j.ijplas.2022.103306.

Dollar, M., Thompson, A.W., 1987. The effect of grain size and strain on the tensile flow stress of quenched aluminum. Acta Metall. 35, 227–235. https://doi.org/10.1016/0001-6160(87)90230-6.

Dou, R., Derby, B., 2009. A universal scaling law for the strength of metal micropillars and nanowires. Scr. Mater. 61, 524–527. https://doi.org/10.1016/j.scriptamat.2009.05.012.

Dunstan, D.J., Bushby, A.J., 2013. The scaling exponent in the size effect of small scale plastic deformation. Int. J. Plast. 40, 152–162. https://doi.org/10.1016/j.ijplas.2012.08.002.

El-Awady, J.A., 2015. Unravelling the physics of size-dependent dislocation-mediated plasticity. Nat. Commun. 6, 5926. https://doi.org/10.1038/ncomms6926.

El-Awady, J.A., Wen, M., Ghoniem, N.M., 2009. The role of the weakest-link mechanism in controlling the plasticity of micropillars. J. Mech. Phys. Solids. 57, 32–50. https://doi.org/10.1016/j.jmps.2008.10.004.

Estrin, Y., Tóth, L.S., Molinari, A., Bréchet, Y., 1998. A dislocation-based model for all hardening stages in large strain deformation. Acta Mater. 46, 5509–5522. https://doi.org/10.1016/S1359-6454(98)00196-7.

Feaugas, X., Haddou, H., 2007. Effects of grain size on dislocation organization and internal stresses developed under tensile loading in fcc metals. Philos. Mag. 87, 989–1018. https://doi.org/10.1080/14786430601019441.

Feaugas, X., Haddou, H., 2003. Grain-size effects on tensile behavior of nickel and AISI 316L stainless steel. Metall. Mater. Trans. A 34, 2329–2340. https://doi.org/10.1007/s11661-003-0296-5.

Fleck, N.A., Muller, G.M., Ashby, M.F., Hutchinson, J.W., 1994. Strain gradient plasticity: theory and experiment. Acta Metall. Mater. 42, 475–487. https://doi.org/10.1016/0956-7151(94)90502-9.

Fourie, J.T., 1968. The flow stress gradient between the surface and centre of deformed copper single crystals. Philos. Mag. 17, 735–756. https://doi.org/10.1080/14786436808223026.

Frank, F.C., Van der Merwe, J.H., 1949. One-dimensional dislocations. I. Static theory. Proc. R. Soc. Lond. A 198, 205–216. https://doi.org/10.1098/rspa.1949.0095.

Frick, C.P., Clark, B.G., Orso, S., Schneider, A.S., Arzt, E., 2008. Size effect on strength and strain hardening of small-scale [111]nickel compression pillars. Mater. Sci. Eng. A 489, 319–329. https://doi.org/10.1016/j.msea.2007.12.038.

Gao, S., Yoshino, K., Terada, D., Kaneko, Y., Tsuji, N., 2022. Significant Bauschinger effect and back stress strengthening in an ultrafine grained pure aluminum fabricated by severe plastic deformation process. Scr. Mater. 211, 114503. https://doi.org/10.1016/j.scriptamat.2022.114503.
Gérard, C., Cailletaud, G., Bacroix, B., 2013. Modeling of latent hardening produced by complex loading paths in FCC alloys. Int. J. Plast. 42, 194–212. https://doi.org/10.1016/j.ijplas.2012.10.010.
Ghorbani Moghaddam, M., Achuthan, A., Bednarcyk, B.A., Arnold, S.M., Pineda, E.J., 2017. Grain size-dependent crystal plasticity constitutive model for polycrystal materials. Mater. Sci. Eng. A 703, 521–532. https://doi.org/10.1016/j.msea.2017.07.087.
Gu, Y., Eastman, D.W., Hemker, K.J., El-Awady, J.A., 2021. A statistical model for predicting size effects on the yield strength in dislocation-mediated crystal plasticity. J. Mech. Phys. Solids. 147, 104245. https://doi.org/10.1016/j.jmps.2020.104245.
Haddou, H., Gaudin, C., Feaugas, X., 2001. Stacking fault energy (s.f.e.) and grain size effects (d) on the tensile behaviour of f.c.c. polycrystalline alloys at 300 K: back stress and effective stress evolutions. Le J. Phys. IV 11. https://doi.org/10.1051/jp4:2001435. Pr4-283-Pr4-291.
Hall, E.O., 1951. The deformation and ageing of mild steel: III discussion of results. Proc. Phys. Soc. Section B 64, 747–753. https://doi.org/10.1088/0370-1301/64/9/303.
Hansen, N., Ralph, B., 1982. The strain and grain size dependence of the flow stress of copper. Acta Metall. 30, 411–417. https://doi.org/10.1016/0001-6160(82)90221-8.
Hielscher, R., Schaeben, H., 2008. A novel pole figure inversion method: specification of the *MTEX* algorithm. J. Appl. Crystallogr. 41, 1024–1037. https://doi.org/10.1107/S0021889808030112.
Hirth, J.P., 1972. The influence of grain boundaries on mechanical properties. Metall. Trans. 3, 3047–3067. https://doi.org/10.1007/BF02661312.
Imrich, P.J., Kirchlechner, C., Motz, C., Dehm, G., 2014. Differences in deformation behavior of bicrystalline Cu micropillars containing a twin boundary or a large-angle grain boundary. Acta Mater. 73, 240–250. https://doi.org/10.1016/j.actamat.2014.04.022.
Jiang, M., Devincre, B., Monnet, G., 2019. Effects of the grain size and shape on the flow stress: a dislocation dynamics study. Int. J. Plast. 113, 111–124. https://doi.org/10.1016/j.ijplas.2018.09.008.
Jiang, M., Fan, Z., Kruch, S., Devincre, B., 2022. Grain size effect of FCC polycrystal: a new CPFEM approach based on surface geometrically necessary dislocations. Int. J. Plast. 150, 103181. https://doi.org/10.1016/j.ijplas.2021.103181.
Kawasaki, Y., 1974. Cell structures in deformed copper single crystals. J. Phys. Soc. Japan 36, 142–148. https://doi.org/10.1143/JPSJ.36.142.
Kiener, D., Motz, C., Dehm, G., 2008. Dislocation-induced crystal rotations in micro-compressed single crystal copper columns. J. Mater. Sci. 43, 2503–2506. https://doi.org/10.1007/s10853-008-2531-3.
Kiener, D., Motz, C., Schöberl, T., Jenko, M., Dehm, G., 2006. Determination of mechanical properties of copper at the micron scale. Adv. Eng. Mater. 8, 1119–1125. https://doi.org/10.1002/adem.200600129.
Kocks, U., Argon, A., Ashby, M., 1975. Thermodynamics and kinetics of slip. Progress in Material Science. Pergamon Press Ltd., pp. 1–47
Koizumi, T., Ogoda, K., Kuroda, M., 2022. Permanent strength of metals: a case study on FCC metals processed by severe plastic deformation. Metall. Mater. Trans. A 53, 2004–2017. https://doi.org/10.1007/s11661-022-06641-1.
Konstantinidis, D.A., Aifantis, E.C., 1998. On the “anomalous” hardness of nanocrystalline materials. Nanostruct. Mater. 10, 1111–1118. https://doi.org/10.1016/S0965-9773(98)00145-7.
Kuhlmann-Wilsdorf, D., 2002. Chapter 59 the LES theory of solid plasticity. pp. 211–342. https://doi.org/10.1016/S1572-4859(02)80010-9.
Lee, S.-W., Nix, W.D., 2012. Size dependence of the yield strength of fcc and bcc metallic micropillars with diameters of a few micrometers. Philos. Mag. 92, 1238–1260. https://doi.org/10.1080/14786435.2011.643250.
Li, S., Sauer, R., Wang, G., 2005. A circular inclusion in a finite domain I. The Dirichlet-Eshelby problem. Acta Mech. 179, 67–90. https://doi.org/10.1007/s00707-005-0234-2.
Li, S., Sauer, R.A., Wang, G., 2007. The Eshelby tensors in a finite spherical domain—Part I: theoretical formulations. J. Appl. Mech. 74, 770–783. https://doi.org/10.1115/1.2711227.
Li, S.-H., Zhao, Y., Kumar, P., Ramamurty, U., 2022. Effect of initial dislocation density on the plastic deformation response of 316L stainless steel manufactured by directed energy deposition. Mater. Sci. Eng. A 851, 143591. https://doi.org/10.1016/j.msea.2022.143591.
Li, Y., Bushby, A.J., Dunstan, D.J., 2016. The Hall–Petch effect as a manifestation of the general size effect. Proc. R. So. A 472, 20150890. https://doi.org/10.1098/rspa.2015.0890.
Lloyd, D.J., Court, S.A., 2003. Influence of grain size on tensile properties of Al-Mg alloys. Mater. Sci. Technol. 19, 1349–1354. https://doi.org/10.1179/026708303225006088.
Lodh, A., Keller, C., Castelluccio, G.M., 2023. Fabrication and mechanical testing of mesoscale specimens. JOM 75, 2473–2479. https://doi.org/10.1007/s11837-023-05857-9.
Madec, R., Kubin, L.P., 2017. Dislocation strengthening in FCC metals and in BCC metals at high temperatures. Acta Mater. 126, 166–173. https://doi.org/10.1016/j.actamat.2016.12.040.
Mathewson, T.K., Douglas, H.T., Ingram, W.T., Castro, L.P., Talcott, T.M.R., Taylor, H.M., 1916. Discussion on the Mexico and Pacific Railroad. Trans. Am. Soc. Civil Eng. 80, 1609–1620. https://doi.org/10.1061/TACEAT.0002781.
Mayeur, J.R., McDowell, D.L., 2013. An evaluation of higher-order single crystal strength models for constrained thin films subjected to simple shear. J. Mech. Phys. Solids 61, 1935–1954. https://doi.org/10.1016/j.jmps.2013.04.007.
McDowell, D.L., 2024a. Nonequilibrium statistical thermodynamics of thermally activated dislocation ensembles: part 3—Taylor–Quinney coefficient, size effects and generalized normality. J. Mater. Sci. 59, 5161–5200. https://doi.org/10.1007/s10853-023-09143-6.
McDowell, D.L., 2024b. Nonequilibrium statistical thermodynamics of thermally activated dislocation ensembles: part 2—Ensemble evolution toward correlation of enthalpy barriers. J. Mater. Sci. 59, 5126–5160. https://doi.org/10.1007/s10853-023-09142-7.
McDowell, D.L., 2024c. Nonequilibrium statistical thermodynamics of thermally activated dislocation ensembles: part 1: subsystem reactions under constrained local equilibrium. J. Mater. Sci. 59, 5093–5125. https://doi.org/10.1007/s10853-023-09165-0.
McDowell, D.L., Liu, Z.-K., 2025. Hierarchical nonequilibrium thermodynamics of thermally activated dislocation plasticity of metals and alloys. Int. J. Plast., 104303 https://doi.org/10.1016/j.ijplas.2025.104303.
Motz, C., Schöberl, T., Pippan, R., 2005. Mechanical properties of micro-sized copper bending beams machined by the focused ion beam technique. Acta Mater. 53, 4269–4279. https://doi.org/10.1016/j.actamat.2005.05.036.
Mughrabi, H., Ungár, T., Kienle, W., Wilkens, M., 1986. Long-range internal stresses and asymmetric X-ray line-broadening in tensile-deformed [001]-orientated copper single crystals. Philos. Mag. A 53, 793–813. https://doi.org/10.1080/01418618608245293.
Müller, M., Zehetbauer, M., Borbély, A., Ungár, T., 1996. Stage IV work hardening in cell forming materials, part I: features of the dislocation structure determined by X-ray line broadening. Scr. Mater. 35, 1461–1466. https://doi.org/10.1016/S1359-6462(96)00319-3.
Nabarro, F.R.N., 1947. Dislocations in a simple cubic lattice. Proc. Phys. Soc. 59, 256–272. https://doi.org/10.1088/0959-5309/59/2/309.
Ng, K.S., Ngan, A.H.W., 2008. Stochastic nature of plasticity of aluminum micro-pillars. Acta Mater. 56, 1712–1720. https://doi.org/10.1016/j.actamat.2007.12.016.
Nye, J.F., 1953. Some geometrical relations in dislocated crystals. Acta Metallurgica 1, 153–162. https://doi.org/10.1016/0001-6160(53)90054-6.
Orowan, E., 1940. Problems of plastic gliding. Proc. Phys. Soc. 52, 8–22. https://doi.org/10.1088/0959-5309/52/1/303.
Oudriss, A., Feaugas, X., 2016. Length scales and scaling laws for dislocation cells developed during monotonic deformation of (001) nickel single crystal. Int. J. Plast. 78, 187–202. https://doi.org/10.1016/j.ijplas.2015.11.003.
Petch, N.J., 1953. The cleavage strength of polycrystals. J. Iron Steel Inst. 25–28.
Qin, W., Li, J., Liu, Y., Kang, J., Zhu, L., Shu, D., Peng, P., She, D., Meng, D., Li, Y., 2019. Effects of grain size on tensile property and fracture morphology of 316L stainless steel. Mater. Lett. 254, 116–119. https://doi.org/10.1016/j.matlet.2019.07.058.
Rubio, R.A., Haouala, S., LLorca, J., 2019. Grain boundary strengthening of FCC polycrystals. J. Mater. Res. 34, 2263–2274. https://doi.org/10.1557/jmr.2019.58.
Saada, G., 2005. Hall–Petch revisited. Mater. Sci. Eng. A 400–401, 146–149. https://doi.org/10.1016/j.msea.2005.02.091.

Sard, R., Weil, R., 1970. Structure of electrodeposited copper single crystals—II. After plastic deformation. Electrochim. Acta 15, 1991–1999. https://doi.org/10.1016/0013-4686(70)85033-2.

Sauzay, M., Kubin, L.P., 2011. Scaling laws for dislocation microstructures in monotonic and cyclic deformation of fcc metals. Prog. Mater. Sci. 56, 725–784. https://doi.org/10.1016/j.pmatsci.2011.01.006.

Scherer, J.-M., Hure, J., Madec, R., Bourdais, F.Le, van Brutzel, L., Sao-Joao, S., Kermouche, G., Besson, J., Tanguy, B., 2024. Tensile and micro-compression behaviour of AISI 316L austenitic stainless steel single crystals at 20 °C and 300 °C: experiments, modelling and simulations. Mater. Sci. Eng. A 900, 146471. https://doi.org/10.1016/j.msea.2024.146471.

Shu, J.Y., Fleck, N.A., 1999. Strain gradient crystal plasticity: size-dependentdeformation of bicrystals. J. Mech. Phys. Solids 47, 297–324. https://doi.org/10.1016/S0022-5096(98)00081-7.

Smyshlyaev, V.P., Fleck, N.A., 1996. The role of strain gradients in the grain size effect for polycrystals. J. Mech. Phys. Solids 44, 465–495. https://doi.org/10.1016/0022-5096(96)00009-9.

Uchic, M.D., Shade, P.A., Dimiduk, D.M., 2009. Micro-compression testing of fcc metals: a selected overview of experiments and simulations. JOM 61, 36–41. https://doi.org/10.1007/s11837-009-0038-2.

Voyiadjis, G.Z., Song, Y., 2019. Strain gradient continuum plasticity theories: theoretical, numerical and experimental investigations. Int. J. Plast. 121, 21–75. https://doi.org/10.1016/j.ijplas.2019.03.002.

Wang, C., Wang, L., Wang, C.-L., Li, K., Wang, X.-G., 2020. Dislocation density-based study of grain refinement induced by laser shock peening. Opt. Laser. Technol. 121, 105827. https://doi.org/10.1016/j.optlastec.2019.105827.

Xiao, Y., Zou, Y., Sologubenko, A.S., Spolenak, R., Wheeler, J.M., 2020. Size-dependent strengthening in multi-principal element, face-centered cubic alloys. Mater. Des. 193, 108786. https://doi.org/10.1016/j.matdes.2020.108786.

Yan, S., Nie, Y., Paradowska, A., 2023. Effect of specimen size and crystallographic orientation on the nano/microscale mechanical properties and deformation behavior of CrCoNi medium-entropy alloy. Mater. Des. 235, 112387. https://doi.org/10.1016/j.matdes.2023.112387.

Zhang, X., Aifantis, K.E., 2011. Interpreting the softening of nanomaterials through gradient plasticity. J. Mater. Res. 26, 1399–1405. https://doi.org/10.1557/jmr.2011.123.

Zhuang, Z., Liu, Z., Cui, Y., 2019. Single-arm dislocation source (SAS)-controlled submicron plasticity. Dislocation Mechanism-Based Crystal Plasticity. Elsevier, pp. 219–237. https://doi.org/10.1016/B978-0-12-814591-3.00008-X.



https://dspace.org/

Mechanistic origin of size effects in crystal plasticity: strain gradients and other theories explained

Nugraha, Arya D.; Castelluccio, Gustavo M.

2025-10-01
Elsevier
https://doi.org/10.1016/j.ijplas.2025.104436
Nugraha AD, Castelluccio GM. (2025) Mechanistic origin of size effects in crystal plasticity: strain gradients and other theories explained. International Journal of Plasticity, Volume 193, October 2025, Article number 104436

Downloaded from a DSpace repository. https://dspace.org/